Available online at www.sciencedirect.com

ScienceDirect

Geochimica et Cosmochimica Acta 71 (2007) 497–520

Geochimica

www.elsevier.com/locate/gca

Shock implantation of Martian atmospheric argon in four basaltic shergottites: A laser probe $^{40}Ar/^{39}Ar$ investigation

Erin L. Walton [a,*], Simon P. Kelley [b], John G. Spray [a]

[a] *Planetary and Space Science Centre, Department of Geology, University of New Brunswick, Bailey Drive, Fredericton, NB, 53B 5A3 Canada*
[b] *Department of Earth Sciences, The Open University, Milton Keynes MK7 6AA, UK*

Received 21 November 2005; accepted in revised form 8 September 2006

Abstract

Spatially resolved argon isotope measurements have been performed on neutron-irradiated samples of two Martian basalts (Los Angeles and Zagami) and two Martian olivine-phyric basalts (Dar al Gani (DaG) 476 and North West Africa (NWA) 1068). With a ~50 μm diameter focused infrared laser beam, it has been possible to distinguish between argon isotopic signatures from host rock (matrix) minerals and localized shock melt products (pockets and veins). The concentrations of argon in analyzed phases from all four meteorites have been quantified using the measured *J* values, $^{40}Ar/^{39}Ar$ ratios and K_2O wt% in each phase. Melt pockets contain, on average, 10 times more gas (7–24 ppb ^{40}Ar) than shock veins and matrix minerals (0.3–3 ppb ^{40}Ar). The $^{40}Ar/^{36}Ar$ ratio of the Martian atmosphere, estimated from melt pocket argon extractions corrected for cosmogenic ^{36}Ar, is: Los Angeles (~1852), Zagami (~1744) and NWA 1068 (~1403). In addition, Los Angeles shows evidence for variable mixing of two distinct trapped noble gas reservoirs: (1) Martian atmosphere in melt pockets, and (2) a trapped component, possibly Martian interior ($^{40}Ar/^{36}Ar$: 480–490) in matrix minerals. Average apparent $^{40}Ar/^{39}Ar$ ages determined for matrix minerals in the four analyzed meteorites are 1290 Ma (Los Angeles), 692 Ma (Zagami), 515 Ma (NWA 1068) and 1427 Ma (DaG 476). These $^{40}Ar/^{39}Ar$ apparent ages are substantially older than the ~170–474 Ma radiometric ages given by other isotope dating techniques and reveal the presence of trapped ^{40}Ar. Cosmic ray exposure (CRE) ages were measured using spallogenic ^{36}Ar and ^{38}Ar production. Los Angeles (3.1 ± 0.2 Ma), Zagami (2.9 ± 0.4 Ma) and NWA 1068 (2.0 ± 0.5 Ma) yielded ages within the range of previous determinations. DaG 476, however, yielded a young CRE age (0.7 ± 0.25 Ma), attributed to terrestrial alteration. The high spatial variation of argon indicates that the incorporation of Martian atmospheric argon into near-surface rocks is controlled by localized glass-bearing melts produced by shock processes. In particular, the larger (mm-size) melt pockets contain near end-member Martian atmospheric argon. Based on petrography, composition and argon isotopic data we conclude that the investigated melt pockets formed by localized *in situ* shock melting associated with ejection. Three processes may have led to atmosphere incorporation: (1) argon implantation due to atmospheric shock front collision with the Martian surface, (2) transformation of an atmosphere-filled cavity into a localized melt zone, and (3) shock implantation of atmosphere trapped in cracks, pores and fissures.

1. Introduction

The composition of the Martian atmosphere was first measured *in situ* by mass spectrometers on board the two Viking landers (Owen et al., 1977). The atmosphere was found to consist of ~95% CO_2 and variable amounts of H_2O, but also contained 2.7% N_2, 1.6% Ar, 0.13% O_2, 2.5 ppm Ne, 0.3 ppm Kr, 0.08 ppm Xe, and trace amounts (ppb) of other reactive gases. The diagnostic signature of the Martian atmosphere has subsequently been discovered in several basaltic and lherzolitic achondrite meteorites (shergottites), confirming Mars as their parent body. This signature, defined by the isotopic ratios of noble gases, N_2 and CO_2, has been linked to the development of shock-induced, glass-bearing melt pockets within these

---

[*] Corresponding author. Present address: University of Alberta, Department of Earth and Atmospheric Sciences, 1-26 Earth Sciences Building, Edmonton, AB, Canada T6G 2E3.
E-mail address: ewalton@ualberta.ca (E.L. Walton).

0016-7037/$ - see front matter © 2006 Elsevier Inc. All rights reserved.
doi:10.1016/j.gca.2006.09.004

meteorites (e.g., Bogard and Johnson, 1983; Becker and Pepin, 1986; Swindle et al., 1986; Wiens et al., 1986; Marti et al., 1995; Bogard and Garrison, 1998, 1999); however, melt pockets are not the only melts produced by shock. Shock veins also occur in strongly shocked Martian meteorites, and are morphologically and genetically distinct from melt pockets. Shock recovery experiments, in which terrestrial basaltic samples were artificially shocked in the presence of an atmosphere, demonstrated the efficiency of shock in producing a glass that contains a sample of the ambient noble gas, with little or no elemental or isotopic fractionation (Bogard et al., 1986; Wiens and Pepin, 1988). The purpose of this study is to spatially resolve between argon isotopic signatures from melt pockets and shock veins in strongly shocked Martian meteorites to constrain the processes responsible for implantation of Martian atmosphere.

A key distinction between Martian and terrestrial noble gases is the high (radiogenic) ^{40}Ar/^{36}Ar and ^{129}Xe/^{132}Xe ratios in the Martian atmosphere. The difference between noble gas isotope ratios in the atmospheres of Mars and Earth is a result of differences in the timing and extent of outgassing between radiogenic noble gases and atmospheric loss. Mars' smaller radius, low gravitational potential and lack of an effective magnetosphere (at least for much of its history) have made the planet particularly susceptible to atmospheric erosion (Catling, 2006). Through a process of large-scale impact events, Mars' atmosphere experienced a period of early atmospheric loss, which stripped atmospheric mass, but did not fractionate gases (Melosh and Vickery, 1989). Solar wind-induced sputtering, whereby neutral atoms in the upper atmosphere become ionized and transported by the interplanetary (solar) magnetic field, was responsible for later fractionation of ^{36}Ar (Jakosky et al., 1994), giving Mars a much lower ^{36}Ar/^{38}Ar ratio (4.0 or less; Bogard, 1997) compared to the terrestrial ratio of 5.3 (Ott, 2002).

The ^{40}Ar/^{36}Ar signature of the contemporary Martian atmosphere, measured from strongly shocked Martian meteorites, lies within the range 1600–1900 (Marti et al., 1995; Bogard and Garrison, 1999; Garrison and Bogard, 2001). The ^{40}Ar/^{36}Ar ratio is of particular relevance to this study, because it is used as an isotopic fingerprint to detect the presence of Martian atmosphere in analyzed samples. Analysis of impact-produced glass separates has shown that this phase hosts a nearly pure component of the Martian atmosphere (e.g., Bogard and Garrison, 1999).

The ^{40}Ar/^{36}Ar ratio for the Martian mantle has been estimated from the trapped component in the crystalline portion of Martian meteorites. Although poorly constrained, it has been estimated to be 300–500 ($\leqslant$300 for ALH 77005, ~300 for Shergotty; Bogard and Garrison, 1999). Using atmospheric argon isotopic compositions, Bogard and Garrison (1999) determined a wide range of ^{39}Ar/^{40}Ar ages for different Martian shergottites. The ages, in general, did not overlap with radiometric ages given by other isotope dating techniques. Bogard and Garrison (1999) concluded that the shergottites incorporated argon with variable ^{40}Ar/^{36}Ar ratios. Although the most intriguing possibility for this component was sampling of a Martian mantle signature, the same effect (higher ^{40}Ar/^{36}Ar ratios) could also result from a combination of Martian atmospheric argon, incorporated terrestrial atmospheric argon, and "inherited" ^{40}Ar, (radiogenic ^{40}Ar that was incompletely degassed when the rock formed, c.f. Swindle, 2002). Previous work has indicated ^{40}Ar/^{36}Ar components in the range 430–680 (EET 79001; Wiens, 1988), and a component <300 (EET 79001; Swindle et al., 1986) thought to represent a Martian interior (mantle) signature.

In this study, laser probe extractions on Martian basalts are interpreted, based on their ^{40}Ar/^{36}Ar ratios, as: (1) Martian atmospheric, if they exhibit high ratios (~1600–1900), (2) Martian mantle, for signatures 300–500, and (3) terrestrial atmospheric contamination for ^{40}Ar/^{36}Ar = 296 (Nier, 1950).

An infrared (IR) laser probe was used to investigate the argon isotopic composition of two Martian basalts: Los Angeles Stone 1 (LA 001) and Zagami, and two Martian olivine-phyric basalts: Dar al Gani (DaG) 476 and North West Africa (NWA) 1068. The IR laser probe was used in this study: (1) to define identify the location and concentration of Martian atmospheric argon, and (2) to constrain the processes that implanted the argon. Cosmic-ray exposure (CRE) ages for the studied meteorites are also reported.

2. Experimental rationale

2.1. Ar–Ar dating

The Ar–Ar dating technique has been applied to several of the known Martian meteorites (35 to date; Meyer, 2006), though spatially resolved (laser probe) analysis has only been undertaken on the orthopyroxenite ALH 84001 (Turner et al., 1997). Stepped heating release data of bulk samples are available for numerous Martian shergottites (e.g., Bogard and Johnson, 1983; Marti et al., 1995; Terribilini et al., 1998; Bogard and Garrison, 1999).

The problem of separating the isotopic signatures of host rock (matrix) minerals and melt pockets using stepped heating techniques can be overcome, to some extent, by the analysis of melt pocket glass and maskelynite separates hand-picked from mineral- and grain-size fractions. Work on hand-picked maskelynite separates has shown that they are dominated by argon derived from decay within the sample, rather than implanted atmospheric gas (Bogard and Garrison, 1999). A disadvantage of stepped heating argon extraction on bulk samples is that it is not possible to distinguish the exact source of the argon because the technique extracts all gases including those trapped in inclusions. In addition, the limited size of shock veins (<200 μm diameter) makes their separation and subsequent analysis using traditional Ar–Ar dating techniques intractable. This method (physical separation of grains) is only suitable for the analysis of larger mm- to cm-size melt pockets, rather than thin shock veins or small melt pockets (µm-size). As Bogard et al. (1986) pointed out, knowledge of the mechanism by which melt pockets form is crucial to understanding how the noble gases are implanted. At the time of their publication, the question of whether the melt pockets formed by *in situ* melting or by injection of extraneous material, remained unresolved.

The laser spot fusion technique for spatially resolved argon isotopic measurement has been applied in this study because of its capacity to analyze heterogeneous samples *in situ*. Using this method, a ~50 µm-diameter laser beam is focused on the sample via an objective lens to outgas argon from discrete volumes (~100–500 µm diameter). This has facilitated the characterization of Martian atmospheric and mantle component reservoirs, in terms of argon isotopes, in melt pockets, shock veins and matrix minerals.

2.2. Sample selection

One purpose of this study was to determine whether shock veins and melt pockets have distinct isotopic signatures. Mineral modes (in vol %), determined by manual point counting on each meteorite thick section investigated in this study, as well as additional thin sections available for analysis (see Section 3), are listed in Table 1. Samples were selected based on their shock state (Fritz et al., 2005) and abundance of localized shock melt products (this study). LA 001 is one of the most strongly shocked Martian basalts (44.4 ± 1.9 GPa; Fritz et al., 2005) and it contains abundant melt pockets (7.8 vol %). These attributes, coupled with the coarse grain size of this meteorite (mm-size maskelynite and pyroxene), make it an excellent candidate for the laser probe. Zagami, NWA 1068 and DaG 476, although more fine-grained than LA 001, are all strongly shocked, in the range 29–43 GPa (Zagami and DaG 476, Fritz et al., 2005; NWA 1068, Walton and Spray, 2003a). These meteorites also contain shock veins, in addition to melt pockets. In terms of vol % of shock melts (shock veins + melt pockets) in the studied sections, Zagami contains 1.2 vol %, NWA 1068 (8.2 vol %) and DaG 476 (9.5 vol %) (Table 1). These meteorites were selected in order to distinguish the isotopic signatures of the two distinct shock melting phenomena (i.e., shock veins versus melt pockets).

Table 1

Modal abundance of major host rock minerals and localized shock melts in the studied meteorites

Phase	Meteorite			
	LA 001	Zagami	DaG 476	NWA1068
Point count	$n = 2500$	$n = 2500$	$n = 3000$	$n = 3000$
Olivine	n.p.	n.p.	18.2	20.0
Clinopyroxene	38.4	70.6	50.2	37.5
Maskelynite	39.5	24.8	19.4	24.0
Opaques	14.3	2.4	2.1	8.8
Melt pockets	7.8	1.2	9.5	8.2
Shock vein	n.p.	1.0	0.6	1.5

n, number of point count measurements averaged; n.p., not present in meteorite.

3. Analytical methods

The analyzed component of each meteorite sample was prepared as a 0.25 mm thick, 1 cm^2 doubly polished thick section (or tile), which was then photographed to provide a map of the distribution of shock veins and melt pockets, and their relationship to matrix minerals. Prior to irradiation, the LA 001 tile was investigated using scanning electron microscopy (SEM) back-scattered electron (BSE) and secondary electron (SE) imaging to characterize microtextures. The remaining three meteorites (Zagami, DaG 476 and NWA 1068) were photographed optically (reflected light). After photography, the tiles were cleaned in Analar methanol and deionized water, wrapped in cadmium foil (to minimize the effects of thermal neutrons) and irradiated in the McMaster Nuclear Reactor, Hamilton (Canada), along with the international biotite standard GA1550, which has a calibrated age of 98.8 ± 0.5 Ma (Renne et al., 1998). Using GA1550 as a fluence monitor, the irradiation parameter, *J*, was determined to be 0.00984 (DaG 476); 0.00985 (NWA 1068); 0.00986 (Zagami), and 0.01175 (LA 001), with errors estimated to be 0.5%. On return, the tiles were placed on an Al platen and loaded into a UHV laser chamber with Kovar window and baked to 120 °C overnight to remove adsorbed terrestrial atmospheric Ar from the samples and chamber walls. Samples remained in the vacuum system for several days prior to analysis to minimize terrestrial atmospheric contamination.

A total of 129 argon extractions were obtained from the four meteorites. Argon isotope data are given in Appendix A. Extraction locations included matrix minerals, melt pockets and shock veins. Extractions were obtained using one to three, one-millisecond laser pulses from a focused Spectron Laser Systems SL902 Nd-YAG laser, which produced a continuous infrared beam with a wavelength of 1064 nm. The beam, having an output of up to 15 W in Transverse Electromagnetic Mode 00 (gaussian distribution of light intensity across the beam), was directed through a customized Leica Metallux 3 microscope using high reflectance, oxide coated mirrors. Hemispherical pits (~100–500 µm diameter) were produced by melting and vaporization at the point of incidence of the laser on the sample surface. The depth of the pit is estimated to be less than half of its diameter (i.e., ~50–250 µm). Following analysis, each tile was turned over to ensure that the laser beam did not penetrate the sample. None of the samples showed any evidence of melting on the opposite side.

Active gases were removed by two SAES AP 10 getters, one operating at 400 °C and one at room temperature. The remaining noble gases were then admitted into the spectrometer and analyzed isotopically for argon only, by a

MAP 215-50 noble gas spectrometer. Argon isotope peak intensities (^{36}Ar, ^{37}Ar, ^{38}Ar, ^{39}Ar, and ^{40}Ar) were measured ten times in sequence over a period of ~15 min. The blank was determined by employing the normal extraction procedures, but without firing the laser. Blanks were run after every two analyses for a period of 5 min. A mean of the day's blanks were used for the blank correction. An example of a photographed tile (DaG 476) and corresponding laser extraction map, illustrated as a sketch of mineral, melt pocket and shock vein shapes, is shown in Fig. 1. DaG 476 was selected as an example because this meteorite contains large mm-size melt pockets (Zagami and NWA 1068 melt pockets are smaller) and shock veins (the LA 001 tile does not contain shock veins).

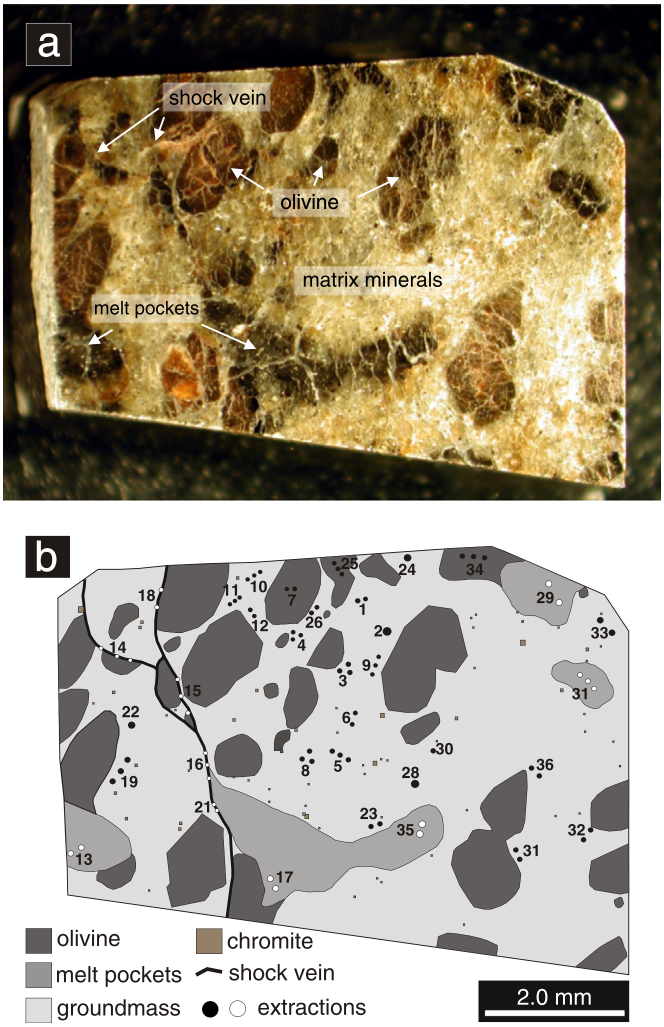

Fig. 1. Reflected light photograph of the dated thick section (tile) from DaG 476 (a) taken prior to irradiation. (b) Sketch of the DaG 476 tile, modified from (a), showing the location of laser probe melt pits. Solid white circles denote argon extractions from shock melts (veins and pockets) and solid black circles denote extractions from host rock minerals (olivine, maskelynite and clinopyroxene). A single circle marks an individual melt pit. Extractions may consist of one, two, or three melt pits, shown as a series of circles with a single number reference. Melt pits are shown roughly to scale. Extractions are numbered in the order in which they were taken.

Corrections for mass spectrometer discrimination and irradiation interferences at masses ^{36}Ar [$(^{36}\mathrm{Ar}/^{37}\mathrm{Ar})_{\mathrm{Ca}} = 0.000265$], ^{39}Ar [$(^{39}\mathrm{Ar}/^{37}\mathrm{Ar})_{\mathrm{Ca}} = 0.00065$], and ^{40}Ar [$(^{40}\mathrm{Ar}/^{39}\mathrm{Ar})_{\mathrm{K}} = 0.0085$] were applied to all argon data following extraction. Data in this paper are presented both uncorrected and corrected for cosmogenic ^{38}Ar and ^{36}Ar. Cosmogenic ^{38}Ar was identified as part of the cosmic ray exposure calculations. ^{36}Ar concentrations were corrected for a cosmogenic component using the following equation:

$$^{36}\mathrm{Ar}_{\mathrm{c}} = {}^{36}\mathrm{Ar}_{\mathrm{m}} \times \left(\frac{1.54 - (^{38}\mathrm{Ar}/^{36}\mathrm{Ar})_{\mathrm{m}}}{1.54 - 0.244} \right)$$

where 1.54 is the ^{38}Ar/^{36}Ar production ratio for cosmic-ray produced noble gases in meteorites (Wieler, 2002), and 0.244 is the ^{38}Ar/^{36}Ar ratio of the Martian atmosphere (Bogard and Garrison, 1999). The subscript c denotes cosmogenic and m denotes the measured ratio. This equation assumes no contribution from chlorine, the implications of which are discussed in Sections 4.1.1 and 6.

For certain Martian meteorites, particularly shergottites, trapped ^{40}Ar dominates the argon isotopic signature rather than radiogenic ^{40}Ar produced *in situ*. ^{39}Ar/^{40}Ar 'ages' therefore, represent apparent ages (Bogard and Garrison, 1999). In such meteorites, measurement of the total argon release is not meaningful and typically provides neither upper nor lower bounds to the crystallization ages/times of argon closure. In this study we present two ages, the first, referred to as 'apparent ages', are ages calculated for individual laserprobe extractions, using the standard equation:

$$t = \frac{1}{\lambda} \ln \left(1 + J \frac{^{40}\mathrm{Ar}^{*}}{^{39}\mathrm{Ar}} \right)$$

where t = time, λ = decay constant (5.543×10^{-10}), J = irradiation parameter and $^{40}\mathrm{Ar}^{*}$ = radiogenic argon (see McDougall and Harrison, 1999; but note that our data were not corrected for terrestrial or Martian atmospheric contamination). Deviation from ages dated by one or more of the Rb–Sr, Sm–Nd and U–Pb chronometers gives a rough estimate of the amount of trapped argon. 'Fitted' or 'average' ages are also reported for each meteorite. These are ages produced by fitting the matrix data on a plot of ^{40}Ar/^{36}Ar versus ^{39}Ar/^{36}Ar to obtain an isochron, or a simple unweighted average age for all analyses.

Thin sections (LA 001, Zagami, DaG 476, NWA 1068) and crystal bond-mounted ultrathin sections (DaG 476, NWA 1068), made from tile off-cuts, were investigated using a JEOL 6400 digital SEM with an EDAX Phoenix X-ray microanalysis system, equipped with a Sapphire Si(Li) detector. SEM analyses were determined at count times of 60 s, beam operating conditions of 15 kV and 1.5 nA, and at a working distance of 14 mm. Analyses were calibrated using a multi-element standards block (Type 202-52) produced by the C.M. Taylor Corporation of Sunnyvale, California. Raster scans, in separate areas of 20 μm × 26 μm, at 5500× magnification, were used to estimate the bulk composition of shock veins and melt pockets (see Walton and Spray, 2003b for analytical details).

4. Laser probe results

Variations in the relative proportions of ^{36}Ar, ^{37}Ar, ^{38}Ar, ^{39}Ar, and ^{40}Ar in the studied meteorites arise from several distinct processes: (1) radiogenic ^{40}Ar produced from the *in situ* decay of potassium; (2) ^{36}Ar and ^{38}Ar (cosmogenic nuclides) produced by interactions of cosmic ray particles with the meteorites, during the time spent in space; (3) ^{36}Ar, ^{38}Ar and ^{40}Ar from the Martian atmosphere, produced by volcanic degassing (and possibly the terrestrial atmosphere); (4) primordial ^{36}Ar, ^{38}Ar and ^{40}Ar from the Martian mantle introduced during accretion of the planet; and (5) ^{37}Ar, ^{38}Ar and ^{39}Ar produced in the McMaster Nuclear Reactor from interfering nuclear reactions during irradiation of Ca, Cl and K, respectively. Corrections have been applied for discrimination, neutron interference reactions, extraction line blanks and spectrometer background peaks (see Section 3).

Data for each meteorite are presented in two plots: (1) ^{40}Ar/^{36}Ar versus ^{39}Ar/^{36}Ar, and (2) ^{40}Ar/^{39}Ar versus ^{36}Ar/^{39}Ar. In the plots of ^{40}Ar/^{36}Ar versus ^{39}Ar/^{36}Ar, ^{36}Ar is not corrected for cosmogenic production (Fig. 2). Data are shown uncorrected in the first plot because the ^{36}Ar content of several matrix samples are dominated by cosmogenic nuclides and the corrected ^{36}Ar points have large errors. Although it may not produce clear isotope correlations, this plot illustrates the distinct argon isotopic ratios in analyses of shock-induced melt products (generally higher ^{40}Ar/^{36}Ar ratios) and matrix minerals (lower ^{40}Ar/^{36}Ar ratios) (see Section 8 for interpretation of this data).

The second plot presented for each sample is ^{40}Ar/^{39}Ar versus ^{36}Ar/^{39}Ar (Fig. 3), where the ^{36}Ar shown has been corrected for cosmogenic production under the assumptions stated in Section 3, concerning cosmogenic and trapped isotope ratios. In this plot, analyses having similar ^{40}Ar/^{36}Ar ratios will be linearly correlated. The plot facilitated identification and measurement of the ^{40}Ar/^{36}Ar ratio in relatively homogeneous reservoirs using a linear fit to the data (G. Turner, private communication). In addition, high ^{36}Ar errors due to corrections for cosmogenic production do not dominate the plot, as would be the case for data normalized to ^{36}Ar. Extractions were excluded from the

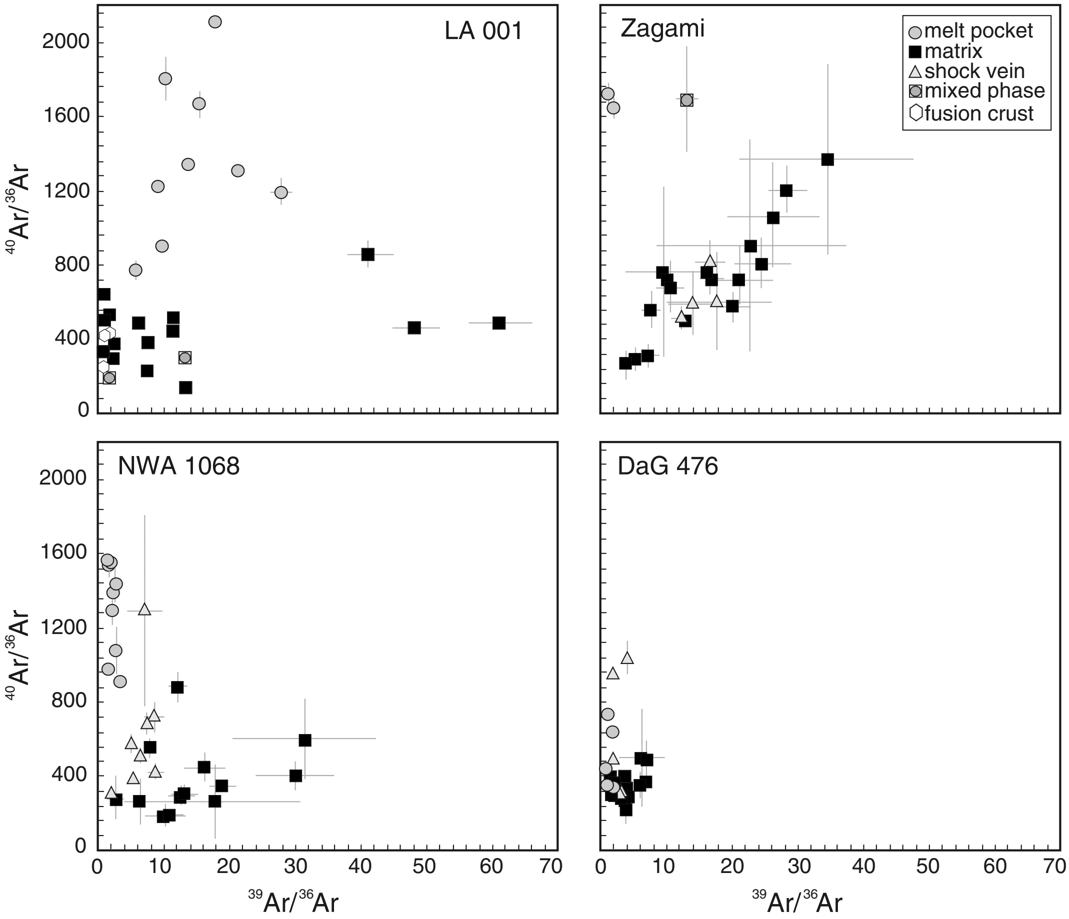

Fig. 2. ^{40}Ar/^{36} versus ^{40}Ar/^{36}Ar isochron diagram for LA 001, Zagami, NWA 1068 and DaG 476. Data have not been corrected for cosmogenic production of ^{36}Ar. For LA 001, extraction 11 (matrix) plots out of the range of data (^{39}Ar/^{36}Ar = 8.26×10^{-11} cc STP). Extractions 11 and 12 (LA 001), and 18 and 19 (Zagami), are not plotted because of large errors. All NWA 1068 and DaG 476 extractions are shown on the plot. Error crosses are 1σ.

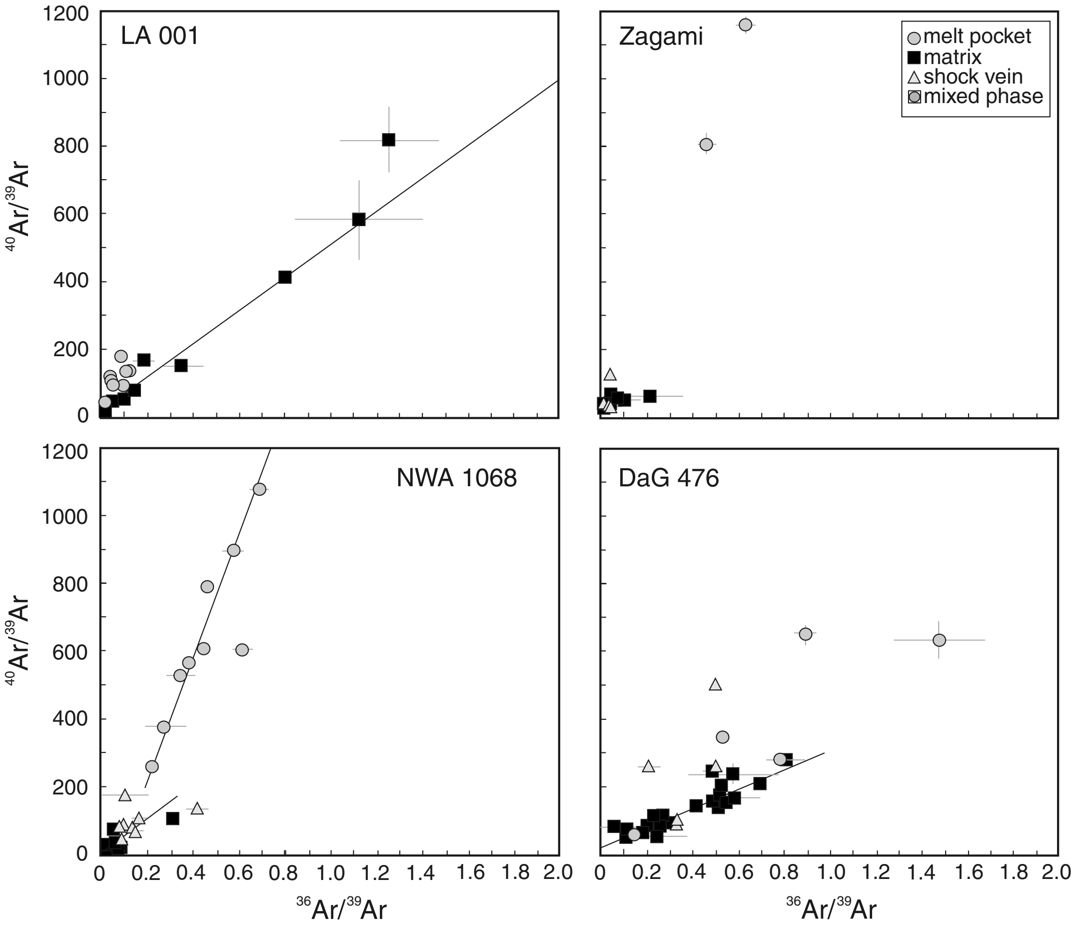

Fig. 3. $^{40}Ar/^{39}Ar$ versus $^{36}Ar/^{39}Ar$ isochron diagram for LA 001, Zagami, NWA 1068, and DaG 476. Data have been corrected for cosmogenic production of ^{36}Ar (see text for details). For LA 001, extractions 4, 5, 6, 10, 11, and 17 were dominated by cosmogenic ^{36}Ar, giving effectively zero ^{36}Ar concentrations after correction (not shown on the plot). Fusion crust extractions (28, 29 and 30), as well as mixed (two-phase) extractions (26 and 27), are not shown on the plot. Extraction 1 was excluded based on the large errors. All matrix data shown on the plot were included in the fit yielding a $^{40}Ar/^{36}Ar$ ratio of 492 ± 28 calculated from the slope. For Zagami, extraction 10 (mixed phase) was excluded from the plot. Extractions dominated by cosmogenic ^{36}Ar (shock vein extraction 18 and 19; matrix extractions 2, 12 and 13) are excluded from the plot. The matrix data shows no spread and is not precise enough to calculate a $^{40}Ar/^{36}Ar$ for this meteorite. All extractions dominated by cosmogenic ^{36}Ar (matrix extractions 2, 7, 8 and 14) are not shown on the plot. All melt pocket and matrix extractions for NWA 1068 have been included in the fit, yielding a $^{40}Ar/^{36}Ar$ ratio of 1839 ± 760 and 485 ± 200, respectively, calculated from the slope. For DaG 476 all matrix data was included in the fit from which a $^{40}Ar/^{36}Ar$ ratio of 286 ± 39 was calculated from the slope. Error crosses are 1σ.

plots if they had high errors, or if the data was insufficiently precise (see expanded figure captions for Figs. 2, 3 and 6 for individual extractions excluded from plots of each meteorite; individual extractions are listed in Appendix A).

4.1. Argon isotopic composition and distribution: Martian basalts

The coarse grain size of Zagami and LA 001, compared to that of DaG 476 and NWA 1068, facilitated the ‘clean’ extraction of argon from matrix minerals using the laser probe. In this context, ‘clean’ extractions are regarded as those that fuse a single phase rather than a mixture of phases. In particular, some of the maskelynite grains exceeded the thickness of the tile (observable due to the transparent nature of maskelynite). Thus, the depth of laser penetration could be constrained to be within a single maskelynite grain. On plots of $^{40}Ar/^{36}Ar$ versus $^{39}Ar/^{36}Ar$ and $^{40}Ar/^{39}Ar$ versus $^{36}Ar/^{39}Ar$ (Figs. 2 and 3), argon extractions from clinopyroxene and maskelynite are plotted with the same symbol, labelled ‘matrix’. Although argon isotopic distinctions between the two matrix minerals are discussed in the following Sections 4.1.1 and 4.1.2, the plots are used primarily to discern argon signatures between shock melts (pocket and veins) and host rock (matrix). The abundance and large diameter of LA 001 melt pockets also allowed for numerous melt pocket extractions, and, additionally, enabled a transect to be taken from the edge of the tile towards the melt pocket margin. The presence of an intact fusion crust in the LA 001 sample (100–500 μm apparent diameter) allowed for analysis of this phase. The Zagami tile contains only 1.2 vol % shock melts (Table 1), thus, only two ‘clean’ extractions from melt pockets were feasible on this sample.

4.1.1. Los Angeles

On the $^{40}Ar/^{36}Ar$ vs $^{39}Ar/^{36}Ar$ diagram (Fig. 2) melt pocket data exhibit higher $^{40}Ar/^{36}Ar$ ratios than in maskelynite and pyroxene. The concentrations of argon in the pockets are greater than the matrix minerals, sometimes by an order of magnitude. In addition, melt pocket analyses exhibit generally higher $^{39}\mathrm{Ar}/^{36}\mathrm{Ar}$ ratios (~6–28) compared to the majority of analyses from matrix minerals and fusion crust (~0.5–13). Three apparently high matrix $^{39}\mathrm{Ar}/^{36}\mathrm{Ar}$ points are the result of low $^{36}\mathrm{Ar}$ contents.

Melt pocket analyses show a wide range of $^{40}\mathrm{Ar}/^{36}\mathrm{Ar}$ ratios. Most plot with uncorrected $^{40}\mathrm{Ar}/^{36}\mathrm{Ar}$ ratios in the range 800–1800 (average of all nine melt pocket extractions, $^{40}\mathrm{Ar}/^{36}\mathrm{Ar} = 1425$), with one extraction yielding a ratio of 2107 ± 34. When corrected for cosmogenic $^{36}\mathrm{Ar}$ and radiogenic $^{40}\mathrm{Ar}$, this extraction yields a ratio of 3340 ± 85. Although this datum lies within the error limits of Viking measurements ($^{40}\mathrm{Ar}/^{36}\mathrm{Ar} = 3000 \pm 500$), it is an outlier since the next highest corrected value from melt pockets is 2378 ± 136, in line with, but still higher than, other measurements from Martian basalts (i.e., 1600–1900; Marti et al., 1995; Bogard and Garrison, 1999; Garrison and Bogard, 2001). The average corrected $^{40}\mathrm{Ar}/^{36}\mathrm{Ar}$ ratio of LA 001 melt pockets is 1852.

Two anomalously low $^{40}\mathrm{Ar}/^{36}\mathrm{Ar}$ melt pocket ratios of 291 ± 9 and 182 ± 24 (extractions 26 and 27) are mixed melt pocket/matrix analyses (see Section 8.2). These melt pockets are distinct in terms of microtextures (Fig. 4a–d), from other melt pockets analyzed from the LA 001 tile (Fig. 4e and f). The large melt pocket with variable $^{40}\mathrm{Ar}/^{36}\mathrm{Ar}$ ratios (melt pocket traverse, extractions 16–19) is a highly vesiculated schlieren-rich glass containing dendritic olivine crystallites (Fig. 4e and f). Although higher concentrations of argon are found within the pocket compared to matrix minerals, there is no direct correlation between argon concentration and the $^{40}\mathrm{Ar}/^{36}\mathrm{Ar}$ ratio within the melt pocket.

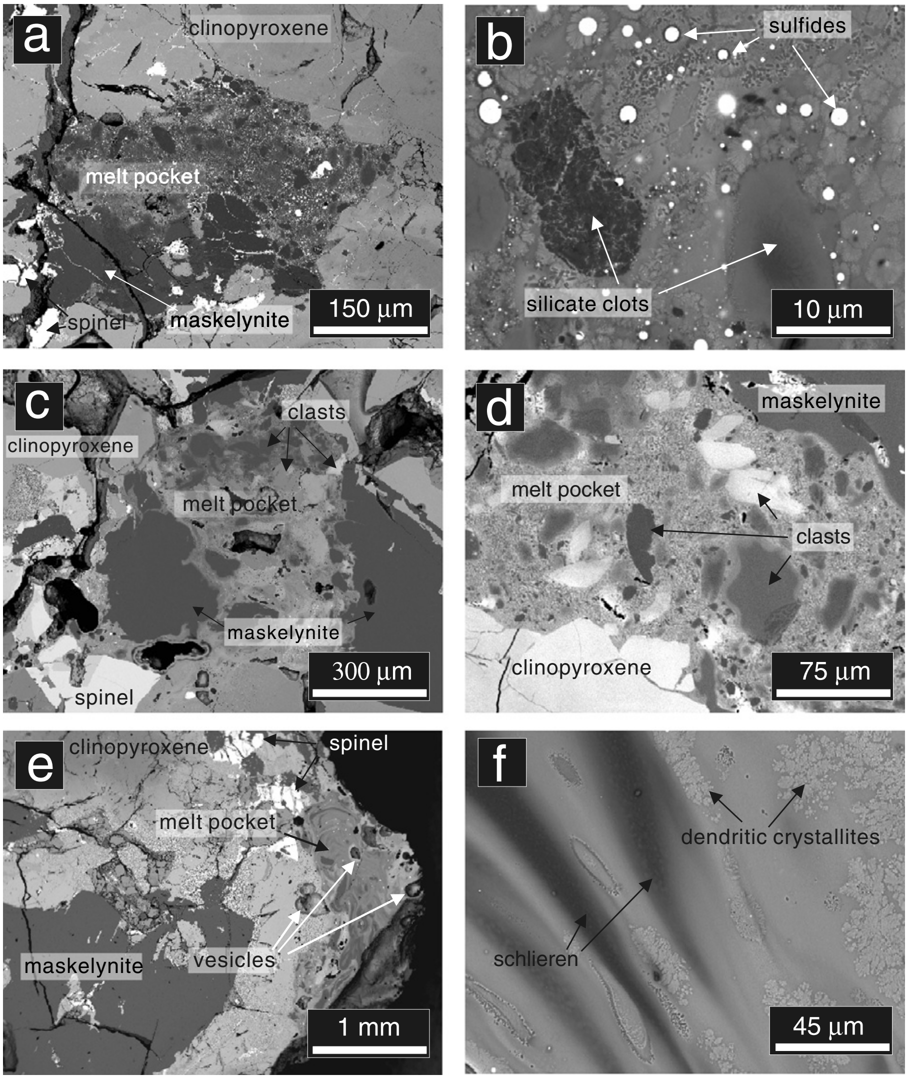

Fig. 4. SEM BSE images of melt pockets from the LA 001 dated tile. (a) Melt pocket Type 1, corresponding to extractions 26 and 27. This melt pocket is characterized by abundant sulfide blebs and rounded clots of unmolten and partially reacted silicate material (b). (c) Melt pocket Type 1, corresponding to Extraction No. 26 and 27. This melt pocket is microcrystalline with abundant clots of unmolten and partially reacted clinopyroxene and maskelynite (d). (e) Large, mm-size Type 3 melt pocket located at the edge of the thick section (note the vesicles in this melt pocket compared to a, b, and c). The melt pocket groundmass is characterized by fine-grained dendritic crystallites embedded in schlieren-rich glass (f).

^{40}Ar/^{36}Ar ratios for matrix minerals are lower than those measured in melt pockets, and range from 126 ± 11 to 855 ± 73 (excluding extractions 1, 11 and 12, which have large errors). Argon in the fusion crust exhibits ^{40}Ar/^{36}Ar ratios ranging from 253 ± 15 to 460 ± 8. Corrected matrix analyses show a linear correlation on a plot of ^{40}Ar/^{39}Ar versus ^{36}Ar/^{39}Ar (see Fig. 3 and expanded caption for extractions used in the fit). A line fitted to this data yields a ^{40}Ar/^{36}Ar ratio = 492 ± 28, representing the trapped component in the rock.

It should be noted that correction of individual extractions in LA 001 for cosmogenic ^{36}Ar production is hampered by variable chlorine contents in the LA 001 meteorite, which result in additional ^{38}Ar from neutron reactions with Cl. This is reflected in the scattered distribution of melt pocket analyses in the ^{40}Ar/^{39}Ar versus ^{36}Ar/^{39}Ar plot (Fig. 3) and several values lying above the line in the CRE plot (see section on Cosmic ray exposure ages for discussion; Fig. 5).

An average apparent ^{39}Ar/^{40}Ar age of 1428 Ma (range 735 ± 5 to 2019 ± 12 Ma) and 1290 (range 159 ± 3 to 4260 ± 94 Ma), resulted from melt pocket and matrix extractions, respectively. In fitting the matrix data (Fig. 2), LA 001 yields a negative age because there are several points with high concentrations of trapped argon. An average age for LA 001 matrix data is 469 ± 210 Ma; however, the lowest age is 188 ± 11 Ma.

4.1.2. Zagami

Uncorrected ^{40}Ar/^{36}Ar ratios for pyroxene grains are in the range ~260–560 and plot at the lower limits of those reported for Zagami maskelynite in this study. Maskelynite analyses show a range of ^{40}Ar/^{36}Ar ratios (295 ± 58 to 1368 ± 513) with ^{39}Ar/^{36}Ar ratios of 6–30. In Zagami, the melt pockets are particularly well distinguished, exhibiting over an order of magnitude greater concentration of ^{36}Ar, and ^{40}Ar/^{36}Ar ratios of 1643 ± 55 and 1724 ± 45 (Fig. 2).

Corrected ^{40}Ar/^{36}Ar ratios for the two melt pocket analyses are 1744 ± 61 and 1830 ± 50, consistent with values from melt pockets in LA 001 (Section 4.1.1) and earlier analyses of impact-produced glass in Martian shergottites (Marti et al., 1995; Bogard and Garrison, 1999; Garrison and Bogard, 2001). On a plot of ^{40}Ar/^{39}Ar versus ^{36}Ar/^{39}Ar, Zagami matrix data are clustered near the zero intercept since they have low radiogenic and trapped components. The lack of spread in the data a line prevented fitting a line to yield a ^{40}Ar/^{36}Ar ratio.

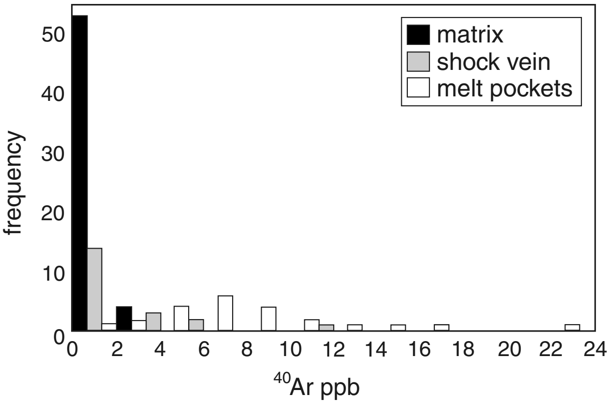

Fig. 5. 40-Argon concentrations (ppb) calculated for matrix minerals, shock veins and melt pockets in LA 001, Zagami, NWA 1068 and DaG 476.

Matrix extractions (maskelynite + pyroxene) yield a scattered array with an average apparent age of 592 ± 57 Ma (range 443 ± 4 to 1039 ± 32 Ma), with low concentrations of ^{36}Ar, much of which was produced by cosmogenic interactions (Appendix A). Shock veins show a similar range of apparent ages (516 ± 12 to 904 ± 15 Ma) and ^{36}Ar contents. Melt pocket extractions yield the highest apparent ages of 3955 ± 31 Ma and 4544 ± 18 Ma. A line fitted to the matrix data on a plot of ^{40}Ar/^{36}Ar versus ^{39}Ar/^{36}Ar (Fig. 2) yields a fitted age of 539 ± 110 Ma.

4.2. Argon isotopic composition and distribution: olivine-phyric Martian basalts

The matrix minerals (maskelynite + pyroxene) of olivine-phyric basalts NWA 1068 and DaG 476 are finer-grained than those of their basaltic relatives (LA 001 and Zagami). Laser probe measurements tended to average maskelynite and pyroxene, representing a mixture of variable portions of these two phases. Olivine was easily avoided because of its coarse grain size (mm-diameter).

DaG 476 proved difficult to analyze due to the degree to which the melt pockets have been replaced by secondary (terrestrial) calcite. The laser also interacted differently with the sample when calcite was encountered; the resultant laser melt pit was highly vesicular, probably as a result of higher concentrations of H_2O and CO_2. Melt from the pit splashed in an approximately mm-sized halo around the pit. This was different than the typical rounded pits with smooth rim profiles produced by melt pockets that did not contain calcite and/or hydrous weathering products, as observed in the other analyzed meteorites (LA 001, Zagami, NWA 1068). Despite the difficulty arising form terrestrial contamination of DaG 476, some general observations can be made from the data (Section 4.2.2).

4.2.1. North West Africa 1068

The three components analyzed from NWA 1068 (shock veins, melt pockets and matrix minerals) have clearly distinguishable ^{40}Ar/^{36}Ar ratios (Fig. 2). In terms of ^{40}Ar/^{36}Ar and ^{39}Ar/^{36}Ar uncorrected ratios, NWA 1068 shock veins show a transitional relationship between melt pocket and matrix analyses (Fig. 2). Uncorrected for cosmogenic nuclides, ^{40}Ar/^{36}Ar ratios of melt pockets (average of all nine extractions = 1307) are up to an order of magnitude greater than in the matrix (average of all 15 extractions = 382).

Although the uncorrected melt pocket ratios appear to vary (Fig. 2), they fall on a single array when corrected for

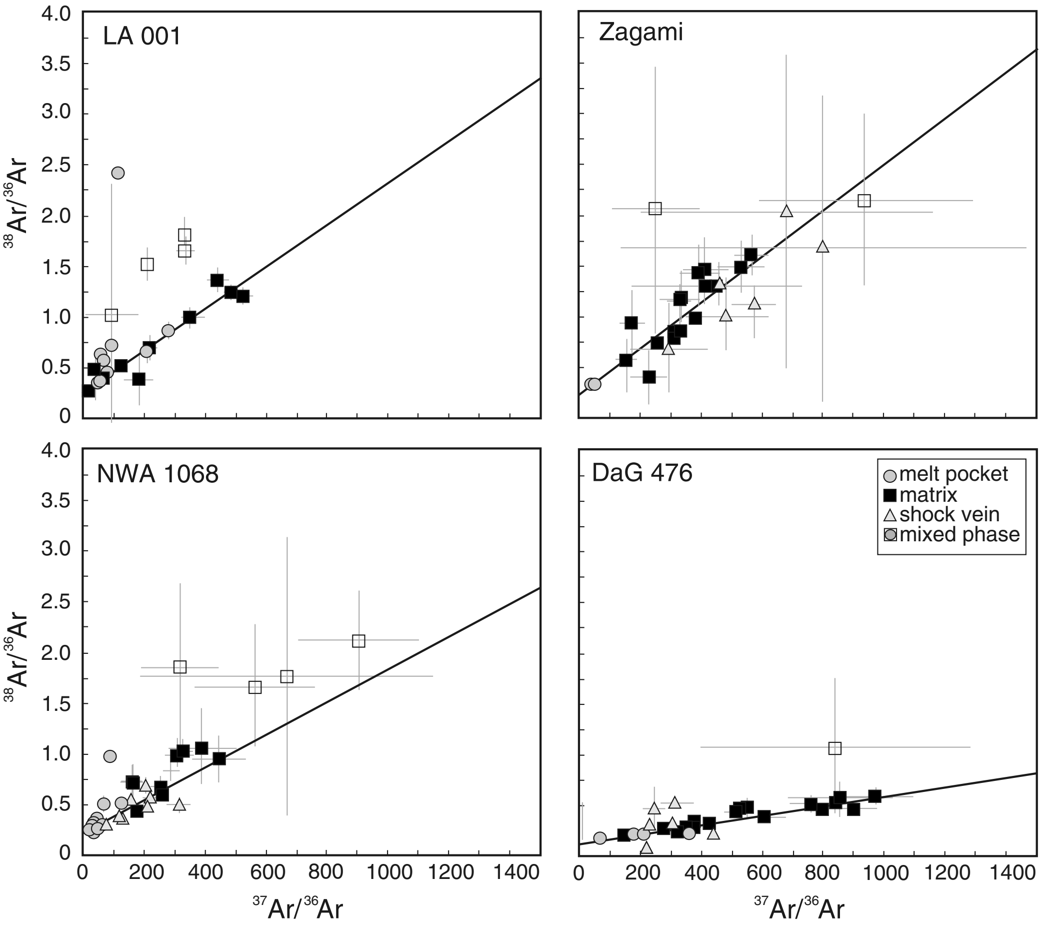

Fig. 6. ^{38}Ar/^{36}Ar versus ^{37}Ar/^{36}Ar isochron diagram for LA 001, Zagami, NWA 1068, and DaG 476. For all four plots, solid matrix symbols denote extractions included in the fits and open symbols are used for extractions not included in the fits. For LA 001, analyses were excluded from the fit if the errors were large, or if the data were not precise enough (matrix spots 4, 5, 12 and 10). Extraction No. 11 plots out of the range of the limits of the figure with large errors. All data points for Zagami are shown on the diagram. Matrix extractions 2, 12 and 23 were not included in the fit. All data points for NWA 1068 are shown on the diagram, extraction numbers 8, 14, 7 and 2, all with high errors, were excluded from the fit. For DaG 476 the only matrix extraction not included in the fit is number 6. Error crosses are 1σ.

cosmogenic ^{36}Ar on a plot of ^{40}Ar/^{39}Ar versus ^{36}Ar/^{39}Ar plot (apart from one point). A ^{40}Ar/^{36}Ar ratio of 1839 ± 760, is calculated from the slope of the line fitted to the melt pocket data (Fig. 3). A line fitted to NWA 1068 matrix data has a slope of 485 ± 200 (^{40}Ar/^{36}Ar ratio) (see Fig. 3 caption for individual data points excluded from the fit). This ^{40}Ar/^{36}Ar ratio falls within the limits of LA 001 matrix data (Fig. 3), and also the terrestrial atmospheric ratio (296).

Apparent ages calculated for individual melt pocket extractions yield the oldest ages, ranging from 2308 ± 15 to 4439 ± 22 Ma. For matrix minerals, individual extractions give an average apparent age of 400 ± 110 Ma (range 291 ± 13 to 1306 ± 15 Ma). A fitted age of 90 ± 160 Ma is obtained by fitting a line to the matrix extractions in Fig. 2. The high error reflects the high concentrations of non-radiogenic components.

4.2.2. *Dar al Gani 476*

The pattern of ^{40}Ar/^{36}Ar ratios in DaG 476 is similar to Zagami and NWA 1068. In general, matrix minerals yield the lowest ^{40}Ar/^{36}Ar ratios (334, average of 24 extractions) while shock veins and melt pockets yield the highest ^{40}Ar/^{36}Ar ratios (565, average of all 10 shock melt extractions; see also Fig. 2).

The highest corrected ^{40}Ar/^{36}Ar ratio measured in a DaG 476 melt pocket was 730 ± 13 (Fig. 3), in contrast to the ^{40}Ar/^{36}Ar values for measured in the other three meteorite samples (974–3340 for LA 001; 1744 and 1830 for Zagami; 986–1696 for NWA 1068). Two of the shock vein analyses reached ^{40}Ar/^{36}Ar ratios of 1010 ± 13 and 1251 ± 133 (Fig. 3).

Matrix mineral data, corrected for production of cosmogenic ^{36}Ar, have a ^{40}Ar/^{36}Ar ratio of 286 ± 39 that lies within error of a terrestrial atmospheric signature (calculated by fitting a line to the matrix data; Fig. 3). The corrected melt pocket data show considerable scatter and a line could not be fitted to obtain a ^{40}Ar/^{36}Ar ratio from the slope.

Apparent ages, calculated for individual matrix extractions, have an average age of 1427 Ma (range 774 ± 7 to 3613 ± 26 Ma) compared to shock melts (veins + pockets), which exhibit an average apparent age of 2324 Ma (range

806 ± 43 to 3613 ± 26 Ma). A line fitted to the matrix data on a plot of ^{40}Ar/^{36}Ar versus ^{39}Ar/^{36}Ar yields a fitted age of 226 ± 320 Ma.

5. Argon distribution and concentration

Previous studies of noble gases in melt pockets within shergottites have shown them to be of Martian atmospheric origin (Bogard and Johnson, 1983; Wiens and Pepin, 1988; Bogard et al., 1989), with some cosmogenic argon which resided in pore spaces following ejection. However, no previous attempt has been made to determine whether the high concentrations are limited to melt pockets, or extend to shock veins.

The *in situ* argon analyses performed in this study allow us to estimate the concentrations of argon in the melt pockets and compare them with concentrations in shock veins and matrix minerals. Argon-40 concentration (by mass) is determined using the measured *J* values, ^{40}Ar/^{39}Ar ratios and K_2O wt% oxide concentrations of individual phases (determined by EDS analysis). Results for individual extractions and a sample calculation are given in Appendix B.

Although the values are scattered, they confirm higher concentrations of Martian atmospheric argon in the melt pockets (2–24 ppb; averages for LA 001, 7.1 ppb; Zagami, 19.7 ppb; NWA 1068, 8.6 ppb; DaG 476, 4.6 ppb) compared with the shock veins and matrix minerals, which have, on average, an order of magnitude less argon (0.3–3 ppb; averages for LA 001, 1.1 ppb; Zagami, 1.2 ppb; NWA 1068, 0.9 ppb; DaG 476, 1.3 ppb) (Fig. 5). DaG 476 presents an exception because the melt pockets are largely replaced by secondary terrestrial calcite. Even though the melt pockets in LA 001 are larger, NWA 1068 and Zagami have equally high and more homogeneous Martian atmospheric argon components.

Although the melt pockets did not acquire their Martian atmosphere via equilibrium processes, it is useful to compare the ^{40}Ar concentrations by considering the pressure of Martian atmosphere that would have been required to yield the observed ^{40}Ar concentrations in the melt (see Appendix B for individual calculations). This can be assessed by making reasonable assumptions about the atmospheric Ar pressure at the Martian surface (1.0^{-4} bars; Kieffer et al., 1992), and Ar solubility in basalt (4.0×10^{-5} cc STP/g per bar; Carroll et al., 1994). For melt pockets, the overpressures required are as much as 3200 times the contemporary Martian atmospheric pressure. Melt pockets in LA 001, Zagami and NWA 1068 require, on average, 1000, 2765 and 1288 times atmospheric pressure, respectively. Assuming a spherical shape for melt pockets, this means that 2–3 L of atmosphere would have to be accommodated in 1 cm^3, with all of the argon dissolved in the melt, in order to achieve the estimated ^{40}Ar concentrations. In contrast, the concentrations in the shock veins would require a few hundred atmospheres overpressure or less (as low as 60 in Zagami).

6. Cosmic ray exposure ages

A three-isotope plot of ^{38}Ar/^{36}Ar versus ^{37}Ar/^{36}Ar for each meteorite is presented in Fig. 6 and can be used to estimate CRE ages. ^{36}Ar and ^{38}Ar are produced by cosmic ray bombardment of several major elements in shergottites (K, Ca, Ti, and Fe), though both are naturally present in Earth's atmosphere and produced by neutron irradiation of Ca and Cl, respectively. ^{37}Ar in the samples is produced by neutron irradiation of Ca ($t_{1/2} = 35.1$ days). The fitted line (Fig. 6) for each sample represents mixing between trapped gas (with low ^{38}Ar/^{36}Ar ratios, dominated by the gas-rich melt pockets) and pure end member spallogenic (cosmic ray produced) gas (higher ^{38}Ar/^{36}Ar ratios, dominated by matrix data points). The spallogenic production ratio ^{38}Ar/^{36}Ar is 1.54 (Wieler, 2002, and references therein), the value appropriate for the elemental composition of Martian meteorites and typical meteoroid shielding, which includes ^{36}Ar produced by decay of cosmogenically produced ^{36}Cl, which decays to ^{36}Ar. Thus, the point at which the fitted line crosses the $^{38}\text{Ar}/^{36}\text{Ar} = 1.54$ line, yields the ^{38}Ar/Ca ratio from which the cosmic ray exposure age can be calculated with simplifying assumptions for rocks with a basaltic composition. Hohenberg et al. (1978) showed that the main target elements producing ^{38}Ar from cosmic ray irradiation were K, Ca, Ti and Fe in the approximate ratio 1.00:1.00:0.14:0.03 with shielding around 10 g/cm^2. The ratios change with varying shielding but not significantly from the above values in comparison to the errors on individual ages. Cosmic ray irradiation of meteorites of basaltic composition is dominated by the target elements Ca and Fe as a result of their abundance. The ratio Ca/Fe in the analyzed shergottites ranges from 0.386 (NWA 1068; Barrat et al., 2002) to 0.588 (Zagami; McCoy et al., 1992) and thus the rate of ^{38}Ar production from Ca and Fe is roughly in the proportions 1.00:0.06, and the production from Fe thus has minor significance in these calculations. A more important issue pertaining to the precision and accuracy of ^{38}Ar cosmic ray ages is the presence of trace amounts of chlorine in some of the samples, which produces ^{38}Ar during neutron irradiation, resulting in scatter of the data with anomalously high ^{38}Ar/^{36}Ar in some analyses.

The CRE age was calculated using a ^{38}Ar production rate of 3.2×10^{-8} cc STP/g Ca/Ma, appropriate to the basaltic composition and assuming that these meteorites had similar shielding and location within the solar system. This production rate is derived from the data of Hohenberg et al. (1978) and more recent work on bulk analyses of H chondrites with known compositions (Leya et al., 2001). In fitting the lines the correlation coefficients for DaG 476 and Zagami samples were high (i.e., there is little scatter in the data), whereas LA 001 and NWA 1068 had appreciable scatter, with both yielding anomalously high ^{38}Ar/^{36}Ar data points resulting from chlorine interference. For both meteorites (LA 001 and NWA 1068), the mixing line was defined by excluding anomalously high points

(^{38}Ar/^{36}Ar ranging from 1.5 to 1.8 for LA and ^{38}Ar/^{36}Ar within 0.7–1.2 for NWA; see Fig. 6 caption). The calculated CRE ages derived using this technique are: LA 001 (3.1 ± 0.2 Ma), Zagami (2.9 ± 0.4 Ma), NWA 1068 (2.0 ± 0.5 Ma), and DaG 476 (0.6 ± 0.1 Ma).

The cosmic ray exposure data also yielded initial ^{38}Ar/^{36}Ar ratios that depart from the terrestrial value in all cases. DaG 476 yields an anomalously low ^{38}Ar/^{36}Ar value of 0.123 ± 0.038 and also a CRE age lower than other determinations on this meteorite (1.24 ± 0.12 Ma; Zipfel et al. 2000). The difference in age and intercept is probably the result of additional ^{37}Ar produced from calcite, which formed in veins on Earth as a result of alteration. The additional ^{37}Ar (from calcite with no cosmic ray bombardment record) would increase ^{37}Ar/^{36}Ar ratios of DaG 476 without changing the ^{38}Ar/^{36}Ar ratios, reducing the intercept and the slope of the fitted line. The cosmic ray exposure age is thus artificially lowered by such alteration, which makes the line meaningless despite the high correlation coefficient. The other three samples all yield non-terrestrial ^{38}Ar/^{36}Ar values of 0.224 ± 0.025 for NWA 1068, 0.198 ± 0.020 for LA 001, and 0.221 ± 0.040 for Zagami. Although all three overlap the terrestrial value (0.188) within errors, they are also all higher and close to the suggested value of 0.256 or greater for Martian atmosphere (Bogard, 1997). However, there is no evidence in these analyses for values much above 0.25 in the Martian atmosphere. Even the most gas-rich pocket analyses, corrected for cosmogenic production, lie below 0.25. Substantial terrestrial contamination is precluded by the high ^{40}Ar/^{36}Ar values from the same analyses.

7. Petrography of shock melts

Two distinct products of shock melting have been observed in the studied meteorites: melt pockets and shock veins. Melt pockets, isolated subrounded to rounded pockets of silicate glass and crystallites, have only been described from strongly shocked Martian meteorites (>29 GPa). Analogous features have not yet been observed in naturally shocked rocks from terrestrial impact craters, nor in controlled laboratory shock-recovery experiments (Table 2). In hand specimen, melt pockets appear as irregularly shaped dark brown to black inclusions, which crosscut igneous minerals. These localized regions of melting occupy up to 11.3 vol % of strongly shocked Martian meteorites (Table 1) and are self-contained, at least within the two dimensions of the thin section (i.e., compound melt pockets were not observed, nor were overlapping melt pockets). Melt pockets are remarkably heterogeneous in terms of composition and texture. For descriptive purposes, melt pockets have been grouped into three types, based on petrographic observations of Walton and Spray (2003b). Smaller (<0.25 mm) Types 1 and 2 pockets tend to be clast- and crystallite-rich, whereas large (mm-size) Type 3 pockets tend to be clast-poor and highly vesiculat-

Table 2
Summary of localized melting phenomena observed in the studied meteorite suite

Type	Morphology (cross section)	Diameter (μm)	Constituents	Range % phases	Contact with host rock	Occurrence	Peak shock (GPa)
Melt pocket	Rounded to subrounded, localized, heterogeneous distribution in host rock	100–4500	Dendritic crystallites Glass Vesicles Clasts Sulfide blebs High-P polymorphs	10–55 2–35 0–25 0–10 0–30 0–5	Gradational, locally intrusive, restricted to grain boundaries	Restricted in occurrence to strongly shocked Martian meteorites	29–55
Melt film	Thin veinlets, localized, heterogeneous distribution in host rock	<5	Glass	100	Gradational, restricted to grain boundaries	Achondrites shock-recovery experiments strongly shocked Martian meteorites	>25
Melt vein	Wedge-shaped veins, localized, emanate from a subsidiary melt pocket	1–60	Glass Sulfide veins + blebs Vesicles	80–95 5–10 5–35	Sharp, cross-cutting, offset/truncates host phases	Strongly shocked Martian meteorites	>25
Shock vein	Intersecting network of veins surrounding unmolten host rock, transects entire specimen	2–200	Glass Clasts Vesicles Sulfide blebs High-P polymorphs	70–100 0–20 0–10 0–10 0–5	Sharp, cross-cutting, offset/truncates host phases	Achondrites, ordinary chondrites, naturally shocked terrestrial rocks, shock-recovery experiments, frictional welding experiments	0–45

Peak shock (GPa) refers to the equilibration shock pressure recorded in host rock maskelynite (Fritz et al., 2005).

ed, typically containing dendritic crystals embedded in a glass matrix. Based on petrographic descriptions the melt pockets analyzed in this study are Types 1 and 3. Melt pockets (all types) are interpreted to be the products of shock melting based on: (1) crosscutting relationships with igneous textures and overprinting by terrestrial alteration (e.g., calcite veins) (Walton and Spray, 2003b), (2) increase in the intensity of bulk shock features approaching small melt pockets (e.g., planar fractures, mosaicism; Treiman et al., 1994; Walton et al., 2005), (3) absence of mechanical shock defects in host rock olivine in direct contact with large (mm-size) melt pockets (Ostertag et al., 1984; Walton et al., 2005), (4) a directly proportional relationship between equilibration shock pressure and shock melt abundance (vol %; Walton et al., 2005), (5) the occurrence of high-pressure phases in some melt pockets (Beck et al., 2004), and (6) the diagnostic signature (in terms of absolute elemental abundances and isotopic ratios) of the Martian atmosphere found in melt pockets of several Martian meteorites (e.g., Bogard and Johnson, 1983; Marti et al., 1995; Bogard and Garrison, 1998). The latter line of evidence relies, in part, on the ability of shock-recovery experiments to demonstrate that hypervelocity impact provides a viable mechanism for implanting a sample of ambient gas in melts produced during shock, without elemental or isotopic fractionation (Bogard et al., 1986).

Microtextural and compositional characteristics have been used as the main criteria for determining the mechanism of melt pocket formation. The contact between host rock minerals and melt pockets is characterized in Table 3. A quantitative method for calculating the proportions of minerals from major element analyses of melt pocket bulk compositions was applied using MINSQ, a least squared spreadsheet method using the *Solver* analysis tool in Microsoft Excel™ (Herrmann and Berry, 2002). For all four meteorites (LA 001, Zagami, NWA 1068 and DaG 476), melt pocket bulk compositions have been reproduced involving variable proportions of host rock phases, reflecting local mineral-scale melting (Table 4).

Table 3
Description of textures observed in a transect across a host rock/melt pocket contact

Host rock → Type 1 melt pocket
- increase in abundance of planar fractures
- decrease in birefringence (clinopyroxene)
- distinct darkening/brown colouration (clinopryoxene/olivine)

Host rock → Type 3 melt pocket
- zone of recrystallization ~1 - 20 mm-thickness
- curvature of twin lamellae
- increase in volume of grain boundary melting
- stringers of normal (non-diaplectic) glass intermingling with melt
- nucleation of crystals from host rock edge into glass

Melt pocket (Types 1 and 3) → host rock
- increase in clast abundance
- decrease in grain size
- progression from swallowtail to feathery morphology (coarsest melt pocket only)

Melt pockets are interpreted to have formed by the localized *in situ* melting of host rock phases based on the following observations:

(1) The interface between host rock minerals and melt pockets is gradational, and only locally intrusive. Melt pockets do not show any evidence for a frictional origin in the form of offsets or displacements of neighbouring phases. Injected melt would be expected to exhibit sharp crosscutting relationships with the host rock, with evidence for forceful injection (i.e., displacement and truncations of host rock minerals). This has been observed in many terrestrial impact structures. For example, impact melt injected into the target footwall at Sudbury possesses sharp/discordant contacts with the host rock (e.g., Tuchscherer and Spray, 2002).

(2) The only melt pockets with any mesostasis contribution are all Type 1. This is consistent with melt pockets initiating via grain boundary melting where the mesostasis is more abundant. Thus, smaller melt pockets will posses a greater contribution of mesostasis to their bulk compositions compared to the larger (mm-size; Type 3) melt pockets that have melted approximately the same amount of the mesostasis, but greater proportions of host rock phases. Olivine-phyric basalts do not contain the Si- and alkali-rich mesostasis observed in Zagami and LA 001 (non-phyric) basalts. Instead, Type 1 melt pockets, in general, show a larger contribution from spinel compared to Type 3 melt pockets, although there is considerable overlap. If melt pockets form by shock impedance contrasts, melts would initiate at the grain boundary between phases with contrasting shock impedance (e.g., chromite—an incompressible mineral, and void space). This could account for the elevated Cr_2O_3 contents of melt pockets by preferential melting of chromite in the host rock (Walton and Herd, 2006). Indeed, in shocked ordinary chondrites, Stöffler et al. (1991) observe preferential mobilization of troilite and metal by local melting processes during shock. In general, for basalts and olivine-phyric basalts, as the size of the melt pocket increases their bulk composition approximates that of the bulk rock. However, some of the small melt pockets do not show large deviations from bulk rock compositions (e.g., NWA 1068). This is attributed to the fine grain size of host rock minerals (clinopyroxene and maskelynite) in olivine-phyric basalts relative to melt pocket diameter, i.e., for coarser-grained basalts the Type 1 melt pocket diameters (<0.25 mm) are small compared to grain size (3–4 mm). However, the fine-grained nature of the host rock means that even for small melt pockets, a higher portion of minerals are melted and the resultant composition is more representative of the bulk rock.

(3) Melt pockets are restricted to strongly shocked Martian meteorites (29–55 GPa). This indicates that melt pocket formation is related to the intensity of shock suffered by the bulk sample and the type of shock wave interaction required to eject solid rock in excess of 5.0 km/s. This is sup-

Table 4
Summary of mineralogical proportions calculated for each melt pocket bulk composition

Sample No.	Type	qz	ms	mk	aug	pg	ol	wht	ulv	r^2
LA melt pocket 1	1	21.50	33.00	6.20	0.00	17.89	19.27	0.18	1.96	0.05
LA melt pocket 2	3	0.00	0.00	24.70	1.03	68.65	0.19	0.76	1.10	1.60
LA melt pocket 3	1	22.21	7.17	46.83	0.00	22.45	0.00	0.11	1.22	0.19
LA melt pocket 4	3	0.00	0.00	11.56	30.11	15.03	16.47	14.08	10.67	1.12
LA melt pocket 5	1	24.50	0.00	10.95	16.82	0.00	0.00	2.40	40.85	1.30
Zagami melt pocket 1	1	2.26	0.01	41.70	25.37	18.91	1.64	3.66	0.13	0.21
Zagami melt pocket 2	1	0.38	0.03	60.28	17.23	17.74	1.57	2.53	0.25	0.73
NWA 1068 melt pocket 1	1	11.59	0.00	26.20	35.90	0.00	0.00	2.45	22.98	1.70
NWA 1068 melt pocket 2	1	6.44	0.00	14.27	42.74	0.00	24.04	1.50	10.41	1.50
NWA 1068 melt pocket 3	1	6.75	0.00	5.36	59.48	0.00	21.28	0.54	6.33	0.50
DaG 476 melt pocket 1	3	11.77	0.00	14.12	20.81	0.00	50.30	0.27	1.08	0.28
DaG 476 melt pocket 2	3	11.59	0.00	3.31	26.39	0.00	58.35	0.36	0.00	0.50
DaG 476 melt pocket 3	1	10.70	0.74	9.67	23.14	0.84	45.53	0.00	3.32	0.04
DaG 476 melt pocket 4	1	9.98	0.00	6.41	25.81	0.00	41.02	1.82	9.80	2.10

Type, melt pockets types 1 or 2; qz, quartz; ms, mesostasis; mk, maskelynite; aug, augite; pg, pigeonite; ol, olivine; wht, whitlockite; ulv, ulvöspinel. r^2 values represent the sum of residuals for the mixing model. Number of iterations = 10000. Tolerance 0.01%.

ported by the observation that in small melt pockets, the intensity of mechanical shock deformation (planar fractures, mosaicism etc.) increases as the melt pocket is approached. This is consistent with formation of melt pockets by shock excursions focussed as point sources in the wake of the shock front that induced bulk (equilibration) shock damage. If melt pockets were to have originated by the forceful injection of extraneous impact melt along fractures in the host rock, a direct relationship between proximity to the melt pocket and equilibration shock level and intensity within the host rock would not be expected.

Based on detailed SEM BSE, SE and EDS investigation, in conjunction with observations using optical microscopy, it is concluded that melt pockets form by local *in situ* melting of target rock minerals, as opposed to forceful injection of extraneous impact melt along fractures in the host rock.

In terms of their textures, shock veins are characterized by sharp, discordant contacts with host rock minerals, and exhibit schlieren-rich internal textures. Displacement and truncation of neighbouring host rock phases is typically observed at the host rock interface. Shock veins have been studied more extensively than melt pockets: they have been formed in shock-recovery experiments (Kenkmann et al., 2000; Langenhorst et al., 2002) and friction-welding experiments (Spray, 1995; van der Bogert et al., 2003). In addition, natural analogues have been observed in other meteorite types (Stöffler et al., 1991) and in terrestrial impact structures (Thompson and Spray, 1996). The formation conditions of shock veins by slip at high strain rates causing comminution and frictional melting, is well constrained from experimental simulation. The occurrence of shock veins is not restricted to strongly shocked samples (Table 2). Instead, shock veins have been observed in meteorites that record moderate peak shock pressures (as low as 10 GPa), and have been produced in the absence of shock by comminution and friction-melting. Shock recovery experiments, designed to maximize shearing of the sample, were able to produce shock veins at pressures as low as 6 GPa. Based on their occurrence and textural characteristics, shock veins are clearly distinguished from melt pockets.

8. Discussion

8.1. Argon isotopic reservoirs

The studied meteorites show evidence for variable mixing of two distinct trapped noble gas reservoirs. Based upon their respective $^{40}Ar/^{36}Ar$ ratios, one was the Martian atmosphere incorporated mainly in melt pockets, the other trapped in the original basalt, probably derived from the Martian mantle:

(1) For LA 001, a plot of $^{40}Ar/^{39}Ar$ versus $^{36}Ar/^{39}Ar$, corrected for cosmogenic ^{36}Ar, yields a linear array of matrix mineral data with a slope of 492 ± 28 ($^{40}Ar/^{36}Ar$ ratio). This represents a measurement of the ‘trapped’ component in the original rock and overlaps with the estimated $^{40}Ar/^{36}Ar$ isotopic composition of the Martian mantle (<500; Bogard and Garrison, 1999). Melt pocket data do not fall along the array defined by matrix data.

(2) A laser probe transect across a large (mm-size) melt pocket, located at the edge of the LA 001 tile, exhibits changing $^{40}Ar/^{36}Ar$ ratios and concentrations. Although high concentrations of argon are found within the melt pocket, relative to matrix minerals, there is no direct correlation between concentration and the $^{40}Ar/^{36}Ar$ ratio within the melt pocket.

(3) NWA 1068 data fall upon a linear array on the $^{40}Ar/^{39}Ar$ versus $^{36}Ar/^{39}Ar$ plot corrected for cosmogenic ^{36}Ar. The fitted line yields a $^{40}Ar/^{36}Ar$ ratio of 1839 ± 760. This ratio is within errors of those determined for a trapped Martian atmospheric component in melt pocket glass separates from Zagami (1600 ± 100; Marti et al., 1995), and whole rock and mineral separates released by stepwise degassing in a high vacuum furnace (1600–

1900; ALH 77005, EET 79001, Shergotty, Yamato 793605, Zagami; Bogard and Garrison, 1999; Garrison and Bogard, 2001). The matrix mineral analyses for NWA 1068 are consistent with LA 001 matrix data (^{40}Ar/^{36}Ar = 492 ± 28), with a ^{40}Ar/^{36}Ar ratio of 485 ± 200. This value, however, falls within error of the terrestrial atmosphere and Martian mantle, and no real conclusions can be drawn from NWA 1068 matrix data.

8.2. The location of Martian atmospheric argon

The Martian atmosphere is overwhelmingly located in melt pockets, identified by high ^{40}Ar/^{36}Ar ratios corrected for cosmogenic ^{36}Ar (average 1403–1852; excluding DaG 476). Shock veins, although presumably formed during the same impact event and hence temporally associated with melt pocket formation, have argon isotopic signatures (^{40}Ar/^{36}Ar and ^{39}Ar/^{36}Ar ratios) that are distinct from melt pockets with lower concentrations of Martian atmosphere. In the cases of Zagami and DaG 476, shock veins show argon isotopic ratios (^{40}Ar/^{36}Ar and ^{39}Ar/^{36}Ar) similar to matrix minerals. Measurement of the shock vein in NWA 1068 shows that this phase possesses a transitional relationship between matrix minerals and melt pockets, in terms of ^{40}Ar/^{36}Ar and ^{39}Ar/^{36}Ar ratios. This may relate to the duration that the melt pockets remained molten and therefore open to inward diffusion, or to the shorter argon diffusion distances of the veins due to their smaller size (in cross section), which meant that more argon is focused into the melt pockets. Another possibility may be that the shock veins were the result of multiple-slip episodes. Crystallization of shock veins takes place on very short timescales, on the order of nano- to milli-seconds for vein widths of 1–100 μm (Langenhorst and Poirier, 2000). As pointed out by Langenhorst and Poirier (2000), the almost instantaneous crystallization of the melt would prevent relaxation of the stress wave, allowing for additional slip and melting by shear (friction). This could also be a mechanism by which shock veins lose their trapped Martian atmospheric argon signature acquired during shock. Calculated ^{40}Ar concentrations further support the conclusion that the Martian atmospheric component is controlled by shock implantation processes. Melt pockets contain, on average, 10 times more gas (ppb ^{40}Ar) than shock veins and matrix minerals. Thus, although matrix minerals and shock veins contain some trapped Martian atmosphere, the melt pockets are dominated by atmospheric gases.

Two of the melt pockets analyzed from the LA 001 tile are small Type 1 melt pockets (Fig. 4a–d). Texturally, these melt pockets are rich in locally derived host rock clasts, sulfide blebs and crystallites. Argon isotopes measured from these melt pockets show that they possess a much lower trapped Martian atmospheric component (uncorrected ^{40}Ar/^{36}Ar = 182 ± 24 and 291 ± 9; Fig. 2) compared with the larger Type 3 melt pockets (average ^{40}Ar/^{36}Ar = 1425). This is not surprising since measurements of the smaller melt pockets represent a mixture of melt pocket and host rock signatures. In this case, the laser beam did not provide high enough spatial resolution to exclude clasts from the melt pocket analyses (the smallest area analyzed was ~100 μm).

8.3. Other argon signatures

Analysis of fusion crust, present on the exterior of the LA 001 tile, yields a ^{40}Ar/^{36}Ar ratio reflecting loss of Martian gases and incorporation of a terrestrial atmospheric signature (^{40}Ar/^{36}Ar$_{\text{terrestrial}}$ = 296).

8.4. Apparent and fitted ages

The apparent ^{39}Ar/^{40}Ar ages (uncorrected for terrestrial and Martian atmospheric argon), determined for matrix minerals clinopyroxene and maskelynite in the four analyzed meteorites are summarized in Table 5 (see Appendix A for individual calculations). Average apparent ages are older than crystallization ages determined by one or both of the Sm–Nd and Rb–Sr geochronometers (LA 001, 172 ± 8 Ma; Zagami, 180 ± 37 Ma; DaG 476, 474 ± 11 Ma; see compiled data in Nyquist et al., 2001) (NWA 1068, 185 Ma; Shih et al., 2003). This indicates that trapped ^{40}Ar occurs in individual mineral phases and is not restricted solely to the products of shock melting. Fitted ages provide upper limits to the ages that, while not very precise, do agree with the accepted ages for NWA 1068 and DaG 476, and to a lesser extent LA 001. Only Zagami is truly discordant, yielding a fitted age of 539 ± 110 Ma, which is older than the reported crystallization age. Thus, with the exception of Zagami, the fitted ages, however imprecise, do seem to represent real events.

8.5. Igneous crystallization

LA 001 and Zagami were both formed by eruption and emplacement of ~10 m thick lava flows near the Martian surface, which cooled at <0.5 °C/h, based on: (1) detailed petrographic and geochemical investigation (Stolper and McSween, 1979; McCoy et al., 1992, 1999; Rubin et al., 2000; Xirouchakis et al., 2002); (2) cooling rate estimates from TEM studies of the thickness of pyroxene exsolution lamellae (Zagami; Brearly, 1991); (3) dynamic crystallization experiments (Zagami et al., 1979; McCoy and Lofgren, 1996); and (4) crystal size distribution (CSD) studies of pyroxenes (Lentz and McSween, 2000, 2003).

The igneous crystallization history for these two meteorites favours crystallization at depth in the Martian crust. This crystallization scenario of slow cooling for LA 001 is consistent with the interpretation of argon isotopic data in this study. Thus, LA 001 did not degas upon emplacement, but retained a Martian mantle signature in its igneous phases. Although the Zagami data from this study is inconclusive (Fig. 3), Bogard and Garrison (1999) report a trapped ^{40}Ar/^{36}Ar ratio of ~400, which may indicate Martian mantle. Most of the variability in the melt pocket analysis is inter-

Table 5
Sumary Ar results from irradiated samples

Meteorite	^{39}Ar/^{40}Ar age (Ma)	Fitted age (Ma)	CRE age (Ma)	^{36}Ar cc/STP/g 10E−12	Trapped Martian atmosphere	^{40}Ar/^{36}Ar in: Mantle
LA 001	1290	469	3.1 ± 0.2	0.52	1852(974–3340)	~492
Zagami	692	539	2.9 ± 0.4	0.05	1744, 1830	
NWA 1068	515	90	2.0 ± 0.5	0.10	1403(986–1696)	~480
DaG 476	1427	226	0.7 ± 0.3	0.20	521 (356–730)	

^{39}Ar/^{40}Ar ages are reported as an average of ages calculated for individual extractions of matrix minerals. Fitted ages are obtained by fitting a line to the matrix extractions on a plot of ^{40}Ar/^{36}Ar vs. ^{39}Ar/^{36}Ar (see text for details). The fitted ages for LA 001 and Zagami have errors of 210 and 110 Ma, respectively. For NWA 1068 and DaG 476 fitted ages yield large errors (in excess of the fitted age), reflecting the high concentration of non-radiogenic components. Cosmogenic ^{36}Ar is presented as an average of all components analyzed (matrix minerals, melt pockets, shock veins). The ^{40}Ar/^{36}Ar ratio for Martian atmosphere is reported as an average (range) of argon extractions from melt pockets, corrected for ^{36}Ar, as this phase contains a nearly pure sample of the Martian atmosphere. Martian pocket mantle estimates were obtained by fitting a line to the matrix data, corrected for cosmogenic ^{36}Ar, on a plot of ^{40}Ar/^{39}Ar vs. ^{36}Ar/^{39}Ar. ^{40}Ar concentration (cc STP/g) and atmospheric overpressure (bars) have been calculated as follows: ^{40}Ar/^{39}Ar ratio: measured in this study using an IR laser probe $^{40}\text{Ar/K} = (^{40}\text{Ar}/^{39}\text{Ar ratio} * J * 0.0001167)/142.6$, where 0.0001167 is the proportion of ^{40}K in natural potassium, which is dominated by ^{39}K (0.93) and ^{41}K (0.07), and 142.6 is a conversion factor to go from cc of ^{39}Ar measured, to g of potassium in the sample. K_2O wt% oxide: individual phases where analyzed for K_2O using EDS. The values given represent an average of 10 analyses per phase (melt pocket, shock vein, maskelynite). $\text{K\%} = K_2O \text{ wt\% oxide} * 0.83$ $^{40}\text{Ar cc STP/g} = (22414 * {}^{40}\text{Ar/K} * \text{K\%}/100)/40$, where 22414 is the number of cc in a mole of gas and one mole of ^{40}Ar weighs 40 g. $^{40}\text{Ar ppb} = (^{40}\text{Ar/K} * \text{K\%}/100) * 1000000000$ Ar overP bars = (^{40}Ar cc STP/g)/(Ar pressure at the Martian surface) $*$ (Ar solubility in basalt), where the atmospheric pressure of Ar at the Martian surface $= 1.0^{-4}$ bars Ar solubility in basalt $= 4.0 \times 10^{-5}$ cc STP/g per bar.

preted to result from melt inclusions carrying a signature of the Martian mantle in matrix minerals (pyroxene + maskelynite) during formation of the melt pockets.

8.6. Cosmic ray exposure ages

Zagami, NWA 1068 and LA 001 yield CRE ages of 2.9 ± 0.4 Ma, 2.0 ± 0.5 Ma and 3.1 ± 0.2 Ma, respectively, within the range previously determined for these meteorites (Heymann et al., 1968; Terribilini et al., 2000; Nyquist et al., 2001; Eugster et al., 2002; Mathew et al., 2003). DaG 476, however, yielded a younger apparent age (0.6 ± 0.1 Ma) than previously determined (1.24 ± 0.12 Ma; Zipfel et al., 2000), attributed to pervasive calcite alteration formed during terrestrial residence. Excluding erroneously young CRE ages for DaG 476, the studied meteorites have been ejected from the Martian surface in two distinct impact events, one at ~1.5 Ma and the other at ~3 Ma.

8.7. Isotopic measurement of altered meteorites

For DaG 476, lower ^{40}Ar/^{36}Ar ratios, compared to those observed in the less altered (LA 001 and NWA 1068) and unaltered (Zagami) meteorites, reflect the extent of melt pocket alteration. Terrestrial contamination lowers the observed ^{40}Ar/^{36}Ar ratio ($^{40}\text{Ar}/^{36}\text{Ar}_{\text{terrestrial}} = 296$; $^{40}\text{Ar}/^{36}\text{Ar}_{\text{Martian}}$ 1600–1900). Petrographic observations of DaG 476 confirm pervasive alteration of matrix minerals and melt products (shock vein and melt pockets) by an irregular network of fractures, partially infilled by calcite.

8.8. Argon implantation mechanisms

Knowledge of the mechanism by which melt pockets form is crucial to understanding how the noble gases are implanted. Our work indicates that melt pockets are formed by focussed *in situ* melting due to localized shock wave-rock excursions, as opposed to melt injection from an extraneous source. The same applies to shock veins, but with an added frictional contribution to melting (e.g., van der Bogert et al., 2003). Any implantation mechanism must account for the difference between Martian atmospheric concentrations in shock veins, which are an order of magnitude lower than those in the melt pockets. We explore three possible processes:

(1) Argon implantation due to atmospheric shock front collision with the Martian surface. During atmospheric transit of a hypervelocity meteorite or comet, a paraboloidal atmospheric shock front is generated around the projectile. This induces a compressed gas layer between the shock front and the projectile, as well as a bow shock wave and wake behind the moving body. Immediately prior to and during initial projectile impact, this compressed gas sheath is driven into the planetary surface. For hypersonic impact, the atmospheric sheath is likely to be several thousand K and in the form of a plasma. Calculations of gas shock density for a meteoroid entering the Venusian atmosphere yield values several thousand to ten thousand times initial gas density (Takata and Ahrens, 1995). Allowing for the more rarefied atmosphere of Mars, similar compression ratios could be realized below the Martian surface. Again this can be constrained to some extent by discussing the amount which might have been introduced at equilibrium. Given an Ar pressure in the Martian near-surface of 10^{-4} bars, and the Ar solubility in basalt of 4×10^{-5} (cc STP/g per bar), the amount of Ar that could dissolve in the basalt is 4×10^{-9} (cc/STP/g), clearly well below the concentrations seen in the melt pockets ($1.0\text{–}1.6 \times 10^{-5}$ cc/g STP). This is the concentration expected for uncompressed Martian atmosphere. In order to get the requisite high concentrations of Ar, as deter-

mined in this study, the shock melt would have to equilibrate with a 2500× overpressured atmosphere, resulting in an Ar concentration of up to 1.0×10^{-5} (cc STP/g). This would only be achieved if the melt was under pressure long enough for Ar to diffuse into the melt subsequent to the shock event. This would be a minimum value since the melt would tend to lose argon rapidly by exsolving gases as bubbles. A similar process is seen in impact melts at the Earth's surface (Haines et al., 2001). This mechanism of argon introduction also requires the melt zone to be directly connected to the atmosphere via fractures (i.e., an open system), a scenario which could be satisfied by atmospheric bow shock impingement into a fractured near-surface substrate (Fig. 7a). The following scenarios, (2) and (3), are variations on the collapse of void space in the host rock, as discussed in Bogard et al. (1986), Wiens and Pepin (1988), Wiens (1988), and summarized in McSween and Jarosewich (1983), and Pepin and Carr (1988).

(2) Transformation of an atmosphere-filled cavity into a localized melt zone (Fig. 7b). In this scenario, the melt pocket forms at high pressure from a pre-existing atmosphere-filled pore space or vesicle, such that the atmospheric component dissolves in the melt. This model requires that virtually all Ar present in the original cavity be incorporated into the melt regardless of the equilibrium solubility of argon in the basaltic melt. If the cavity has a sphere diameter of 0.1 cm, and the melt a density of 3 g cm^{-3}, and the atmospheric pressure is 10^{-4} bars, then the sphere volume would be 5.2×10^{-4} cm^3, the amount of Ar in the cavity is 5.2×10^{-8} cm^3 and the mass of melt in the cavity is 1.6×10^{-3} g. If all the Ar in the original cavity was incorporated into the melt the concentration would be 3.3×10^{-5} cc/g (almost twice the highest measured concen-

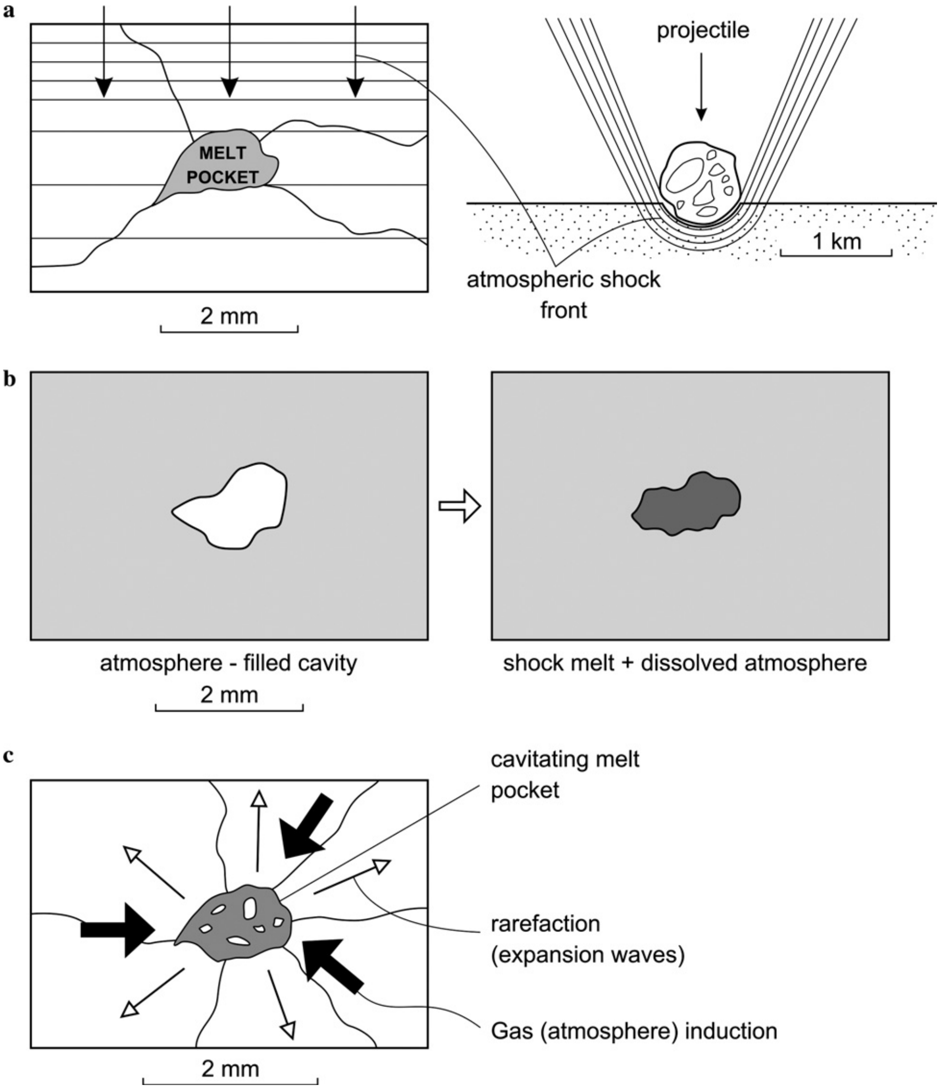

Fig. 7. Sketches illustrating three scenarios for argon implantation. (a) Argon implantation due to shock front collision with the Martian surface. (b) Transformation of an atmosphere-filled cavity into a localized melt zone. (c) Shock implantation of atmosphere trapped in cracks, pores and fissures.

tration). The precise mechanism for this process is unclear, but it would require closed system conditions and yet approximately homogeneous incorporation of the atmospheric component into the melt pocket. This scenario would almost certainly also suffer from the same exsolution and bubble formation seen in scenario (1) as pressures relaxed.

(3) Shock implantation of atmosphere trapped in cracks, pores and fissures (Fig. 7c). This is a variant of (2) above, but involves compression of atmosphere from a larger rock volume into a cavity. A mechanism for pumping atmosphere into melt pockets might be cavitation (Spray, 1999). Once the main shock wave has passed, a rarefaction wave releases the pressure very suddenly and melts present may undergo bubble formation via decompression. The bubble-bearing (cavitated) melt would act as a vacuum and as they relaxed to ambient pressures, atmospheric volatiles in the surrounding volume would migrate into the cavity. The incorporation of argon in the melt would still exceed any equilibrium solubility of argon in basaltic melt. However, the implosion of atmosphere into the melt pocket could generate the high Ar concentrations. This mechanism is compatible with the results of meso- and micro-scale computational investigations of shocked heterogeneous materials (e.g., Crawford and Barnouin-Jha, 2003), where localized extreme shock excursions were generated in the wake of the main shock front (i.e., secondary shock implosions producing temperature and pressure peaks resulting in melt pocket formation).

In the experimental study by Bogard et al. (1986), argon was shock implanted into basaltic powder to a concentration up to 2.5×10^{-3} cc STP/g at 30 GPa shock pressure. This experiment was conducted at 3 atm of argon pressure within the pore space, and the implanted argon concentration was similar to that measured in EET 79001 melt. Under these conditions, the Ar gas was only contained in pore space inside a sealed container that had no free head space, thus, the projectile could not compress an Ar atmosphere in front of it before striking the basaltic target. Yet, significant concentrations of Ar were easily implanted. This argues that scenario (1), projectile compression of injected gas, is not required to explain Martian atmosphere in shock melts. For (2) and (3), void space is required, however, this does not mean that the target rock underwent vesiculation upon emplacement as a lava flow or shallow intrusion. Void space could simply be cracks or fractures in the target rock. It is not possible to discriminate between (2) and (3) for incorporation on the present data alone, though future work combining N_2, CO_2 and Ar, may shed light on this problem.

9. Conclusions

The melt pockets and shock veins of strongly shocked Martian meteorites contain trapped argon with different ^{40}Ar/^{36}Ar ratios. Distinct argon isotopic signatures of shock veins and melt pockets confirm textural observations that melt pockets and shock veins are distinct shock melting features. Compositional and textural observations support melt pocket formation by focussed *in situ* host rock melting during shock. In contrast, shock veins form by comminution and slip at high strain rates and may be active for some seconds after shock wave passage. Although the shock veins do contain some Martian atmosphere, the concentrations are, in general, an order of magnitude less than those observed in the melt pockets. The presence of the same component in different concentrations implies a common mechanism with different trapping efficiencies.

A large scatter in corrected ^{40}Ar/^{36}Ar ratios in the LA 001 melt pockets (974–3340) is the result of incomplete mixing of two gas reservoirs: Martian mantle (480–490) and Martian atmosphere (1403–1852). Zagami, NWA 1068 and, to a lesser extent, DaG 476, show relatively homogeneous argon reservoirs in melt pocket argon isotope data.

The larger (mm-size) melt pockets contain a nearly pure sample of Martian atmospheric argon. Three processes are considered for incorporation: (1) argon implantation due to atmospheric shock front collision with the Martian surface, (2) transformation of an atmosphere-filled cavity into a shock-localized melt zone, and (3) shock implantation of atmosphere trapped in cracks, pores and fissures. We regard the latter two processes as most favorable, whereby melt pockets form by localized *in situ* shock melting introducing atmospheric gases through collapse of void space in the target rock.

Data obtained from Martian meteorites recovered from hot desert environments should be used with caution. In particular, weathering introduces terrestrial noble gases and alteration minerals. Melt pockets and shock veins carrying the signature of Martian noble gas reservoirs are particularly susceptible to alteration because of their amorphous nature.

Acknowledgments

This work has been funded by the Natural Sciences and Engineering Research Council of Canada grants awarded to E.L.W. and J.G.S., Canadian Space Agency supplements to E.L.W., and Leverhulme grant awarded to S.P.K. The J.S. Little Student Travel Fellowship facilitated a three week work-study by E.L.W. in the Argon Laboratory at the Open University, UK. We thank Grenville Turner for his help in understanding the argon components in our samples. We thank Timothy Swindle, Mario Trieloff, and an anonymous reviewer for their reviews of an earlier version of this manuscript. This is Planetary and Space Science Centre contribution 46.

Associate editor: Gregory F. Herzog

Appendix A

Argon-isotopic data for irradiated Martian meteorite samples

Extr. No.	Phase*	$^{39}Ar/^{36}Ar$ uncorrected	±	$^{40}Ar/^{36}Ar$ uncorrected	±	$^{37}Ar/^{36}Ar$ uncorrected	±	$^{38}Ar/^{36}Ar$ uncorrected	±	^{36}Ar cosmogenic	±	$^{40}Ar/^{36}Ar$ corrected	±	$^{40}Ar/^{39}Ar$ corrected	±	Age (Ma)	±
LA 001, J = 0.01175																	
1	px	0.3	0.3	330	91	185	48	0.38	0.26	0.03	0.01	370	110	1200.0	1100.0	4870	1560
2	px	11.0	0.6	446	23	525	28	1.21	0.08	0.05	0.01	1700	340	39.0	0.6	681	9
3	px	7.6	0.3	228	11	483	21	1.24	0.07	0.05	0.01	1000	190	30.0	0.7	545	11
4	px	61.0	4.9	480	40	330	28	1.81	0.17					7.8	0.2	159	3
5	px	48.0	3.5	456	34	335	25	1.65	0.13					9.5	0.1	191	3
6	m.p.	28.0	1.6	1200	71	278	18	0.86	0.08	0.09	0.01	2300	260	43.0	0.3	735	5
7	px	13.0	0.9	126	11	442	32	1.37	0.12	0.02	0.01	940	460	9.4	0.6	189	11
8	px	2.2	0.2	368	25	349	25	0.99	0.10	0.06	0.01	870	130	170.0	6.4	1960	47
9	mk	11.0	1.0	505	46	220	21	0.70	0.12	0.07	0.01	780	110	44.0	1.1	753	15
10	mk	41.0	3.5	855	73	209	18	1.53	0.16					21.0	0.3	393	5
11	mk	83	130	1200	2000	301	480	4.95	8.10					15.0	2.5	295	46
12	mk	26	23	770	700	94	84	1.02	1.30					30.0	4.6	541	72
13	mk	7.6	0.3	367	14	119	5	0.51	0.04	0.22	0.01	460	21	48.0	0.6	809	9
14	mk	2.0	0.2	293	26	208	17	0.65	0.10	0.08	0.01	430	52	150.0	7.3	1830	57
14b	m.p.	18.0	0.3	2110	34	91	3	0.72	0.02	0.38	0.01	3300	85	120.0	1.3	1570	12
15	px	0.8	0.1	640	40	29	2	0.27	0.05	0.19	0.01	650	41	820.0	47.0	4260	94
Begin melt pocket transect																	
16	m.p.	9.7	0.1	890	9	49	1	0.36	0.01	1.20	0.01	970	10	92.0	0.4	1320	6
17	m.p.	21.0	0.5	1300	29	115	5	2.42	0.06					61.0	0.2	976	4
18	m.p.	16.0	0.6	1660	66	56	3	0.64	0.05	0.17	0.01	2400	14707	110.0	0.5	1470	7
19	m.p.	5.8	0.4	764	53	65	5	0.58	0.09	0.10	0.01	1000	95	130.0	2.3	1680	20
20	px	6.1	0.6	479	50	41	5	0.46	0.10	0.08	0.01	570	71	78.0	2.3	1170	26
End melt pocket transect																	
21	px	0.9	0.1	504	40	38	4	0.28	0.09	0.01	0.01	580	43	580.0	58.0	3710	158
22	m.p.	14.0	0.3	1330	24	78	2	0.46	0.02	0.45	0.01	1600	35	96.0	0.2	1360	5
23	px	1.3	0.0	521	2	4	0	0.21	0.00	6.90	0.02	510	2	410.0	1.5	3170	9
24	m.p.	10.0	0.7	1790	520	46	4	0.36	0.08	0.12	0.01	2000	180	180.0	1.5	2020	12
25	m.p.	9.0	0.3	1220	43	29	2	0.27	0.04	0.28	0.01	1200	44	140.0	1.1	1720	11
26	mp + px	13.0	0.4	291	9	291	11	0.92	0.04	0.16	0.01	610	38	22.0	0.3	413	5
27	mp + px	1.7	0.2	182	24	394	45	0.98	0.15	0.04	0.01	420	110	110.0	9.7	1460	92
28	fusion	2.6	0.1	460	8	25	1	0.19	0.02	0.54	0.01	440	8	180.0	2.7	2040	19
29	fusion	1.2	0.0	399	4	52	1	0.26	0.01	1.50	0.02	400	4	330.0	2.3	2860	12
30	fusion	0.8	0.1	253	15	324	19	0.80	0.07	0.10	0.01	450	43	300.0	20.0	2730	95
Zagami, J = 0.000986																	
1	mk	23	14	908	570	448	280	1.29	0.97	0.00	0.01	4600	15000	39.0	1.3	592	17
2	mk	10	6	764	460	247	150	2.04	1.40					79.0	3.2	1040	32
3	mk	25	4	805	140	388	66	1.40	0.28					33.0	0.3	502	5
4	px	4.1	1.1	261	73	225	63	0.38	0.26	0.02	0.01	290	92	64.0	3.2	884	35
6	mk	21	5	722	170	305	74	0.83	0.29	0.01	0.01	1300	580	34.0	0.5	522	7
5	px	7.4	1.4	311	60	410	78	1.44	0.32					42.0	1.1	627	14
7	px	7.9	1.5	562	110	331	65	1.15	0.27	0.01	0.01	1900	1200	71.0	1.7	955	18
8	mk	17.0	1.9	727	81	328	36	1.14	0.16	0.02	0.01	2300	830	43.0	0.6	632	8
9	mk	11.0	2.2	680	240	154	31	0.56	0.21	0.02	0.01	890	140	63.0	1.2	870	14
10	mp + mk	13.0	2.2	1710	280	328	54	0.83	0.19	0.03	0.01	3100	940	130.0	1.1	1470	10

12	mk	35	13	1370	510	934	350	2.12	0.86					40.0	0.4	595	6
13	mk	29	3	1200	120	563	58	1.59	0.19					42.0	0.2	628	3
15	s.v.	17	2	822	110	459	62	1.30	0.21	0.01	0.01	4400	3200	49.0	0.4	707	5
17	s.v.	13	2	519	68	571	74	1.10	0.18	0.02	0.01	500	590	41.0	0.4	609	6
18	s.v.	25	21	1100	110	799	670	1.65	1.50					51.0	1.1	739	13
19	s.v.	30	21	1470	1400	677	480	2.01	1.50					66.0	1.3	904	15
20	s.v.	14	4	595	170	479	140	0.99	0.37	0.01	0.01	1400	950	41.0	0.7	616	10
21	s.v.	18	8	603	270	291	130	0.66	0.44	0.01	0.01	890	580	34.0	0.9	515	12
22	m.p.	2	0	1720	45	44	1	0.32	0.02	0.32	0.01	1800	50	1200.0	11.0	4540	18
23	mk	26	7	1060	290	168	46	0.92	0.33	0.01	0.01	2200	040.0	40.0	0.4	602	6
24	mk	20	3	573	79	526	76	1.48	0.24					28.0	0.3	443	4
25	mk	17	2	762	69	410	38	1.29	0.14	0.02	0.01	3900	1800	46.0	0.3	673	5
26	m.p.	2.0	0.1	1640	55	40	1	0.32	0.03	0.22	0.01	1700	61	810.0	15.0	3960	31
27	mk	5.5	1.1	295	58	305	60	0.77	0.22	0.02	0.01	500	160	54.0	1.4	771	16
28	mk	13.0	1.3	500	47	381	37	0.96	0.12	0.04	0.01	1100	240	38.0	0.4	572	6
29	mk	10.0	1.3	709	91	252	33	0.73	0.14	0.04	0.01	1100	230	68.0	0.8	923	10
NWA 1068, J = 0.00985																	
2	matrix	15.0	3.2	504	110	901	200	2.11	0.49					34.0	1.7	522	23
3	matrix	2.7	0.1	288	8	181	5	0.43	0.02	0.14	0.00	340	11	110.0	1.7	1310	15
5	m.p.	3.5	0.1	917	36	130	5	0.52	0.03	0.12	0.01	1200	57	260.0	2.7	2310	15
6	matrix	10	3	190	66	386	120	1.05	0.38	0.01	0.01	500	410	18.0	3.2	301	49
7	matrix	18	13	262	200	668	480	1.76	1.40					15.0	4.3	242	67
8	matrix	7	3	262	120	320	130	1.85	0.81					41.0	7.1	607	90
9	matrix	11	2	194	35	377	66	1.23	0.23	0.01	0.01	800	580	18.0	0.9	291	13
10	matrix	8.0	0.7	558	46	289	24	0.83	0.08	0.04	0.01	1000	150	70.0	1.0	944	11
11	matrix	12.0	1.0	890	76	257	22	0.61	0.07	0.05	0.01	1200	150	73.0	1.0	982	11
12	matrix	30	6	405	82	444	89	0.95	0.22	0.01	0.01	880	390	13.0	0.4	224	6
13	matrix	19	2	348	33	329	31	1.02	0.11	0.02	0.01	870	200	18.0	0.3	301	4
14	matrix	31	11	605	210	562	200	1.66	0.61					19.0	0.6	313	9
15	s.v.	2.2	0.1	307	16	70	4	0.30	0.02	0.11	0.01	320	18	140.0	1.8	1540	15
16	s.v.	8.6	0.9	720	77	207	22	0.68	0.08	0.04	0.01	1100	1.0	83.0	1.0	1080	10
17	s.v.	7.4	0.7	689	61	218	20	0.56	0.06	0.05	0.01	910	110	93.0	0.6	1170	8
18	s.v.	5.4	0.4	387	29	210	16	0.47	0.04	0.07	0.01	470	43	72.0	0.7	963	9
19	s.v.	8.7	1.0	426	50	313	37	0.49	0.07	0.04	0.01	530	77	49.0	0.4	709	6
20	m.p.	1.9	0.0	1550	36	43	1	0.36	0.01	0.24	0.01	1700	43	800.0	8.8	3930	20
21	m.p.	2.4	0.0	1390	21	44	1	0.1	0.01	0.38	0.01	1500	23	570.0	33	3400	12
22	m.p.	1.4	0.0	1570	37	34	1	0.25	0.01	0.31	0.01	1600	37	1100.0	13.0	4440	22
23	m.p.	2.1	0.1	1310	47	42	3	0.28	0.01	0.16	0.01	1300	49	610.0	5.7	3520	17
24	s.v.	5.2	0.5	575	52	116	11	0.38	0.04	0.06	0.01	640	65	110.0	1.1	1330	11
25	s.v.	6.4	0.6	509	44	133	12	0.36	0.04	0.06	0.01	560	53	79.0	1.0	1040	11
26	m.p.	1.6	0.1	980	29	24	1	0.25	0.01	0.20	0.01	990	29	610.0	6.3	3520	18
27	m.p.	2.8	0.4	1080	130	67	8	0.50	0.07	0.04	0.01	1300	200	380.0	9.1	2820	35
29	matrix	7.6	1.6	166	35	162	34	0.73	0.17	0.03	0.01	450	93	23.0	0.2	370	3
30	matrix	13.0	1.8	304	42	253	35	0.67	0.10					28.0	0.3	436	5
31	s.v.	16.0	3.2	450	88	379	74	1.23	0.25	0.02	0.01	1700	880	180.0	9.2	1830	60
32	m.p.	7.2	2.9	1290	520	157	63	0.54	0.25	0.27	0.01	1600	54	900.0	13.0	4130	25
33	m.p.	1.7	0.1	1530	52	50	2	0.27	0.01	0.11	0.01	1500	130	530.0	12.0	3310	35
34	matrix	2.7	0.2	1440	120	61	5	0.30	0.03	0.03	0.01	690	250	23.0	1.6	374	24

(*continued on next page*)

Appendix A (*continued*)

Extr. No.	Phase*	$^{39}Ar/^{36}Ar$ uncorrected	±	$^{40}Ar/^{36}Ar$ uncorrected	±	$^{37}Ar/^{36}Ar$ uncorrected	±	$^{38}Ar/^{36}Ar$ uncorrected	±	^{36}Ar cosmogenic	±	$^{40}Ar/^{36}Ar$ corrected	±	$^{40}Ar/^{39}Ar$ corrected	±	Age (Ma)	±
DaG 476, J = 0.00984																	
1	matrix	1.3	0.1	355	17	151	7	0.21	0.03	0.12	0.01	350	16	280.0	8.5	2390	41
2	matrix	3.2	0.2	341	20	523	31	0.48	0.05	0.08	0.01	420	30	110.0	2.2	1300	20
3	matrix	6.9	1.4	494	100	852	170	0.57	0.18	0.02	0.01	660	180	71.0	1.9	961	20
4	matrix	1.7	0.3	394	58	368	54	0.30	0.10	0.04	0.01	410	63	240.0	17.0	2170	89
5	matrix	3.9	0.3	345	26	516	40	0.45	0.06	0.06	0.01	410	37	89.0	1.5	1140	15
6	matrix	6	3	501	260	839	440	1.08	0.66					80.0	5.7	1040	57
7	olivine	3.8	1.0	209	56	14	4	0.34	0.19	0.02	0.01	230	65	55.0	3.7	777	43
8	matrix	1.7	0.2	279	22	273	23	0.29	0.06	0.07	0.01	290	24	170.0	6.6	1760	44
9	matrix	4.2	0.4	277	25	759	68	0.52	0.08	0.05	0.01	350	41	67.0	1.3	911	15
10	matrix	1.8	0.1	259	15	223	14	0.30	0.04	0.09	0.01	270	17	140.0	3.7	1560	28
13	m.p.	1.9	0.0	640	8	359	6	0.25	0.03	0.21	0.00	640	8	350.0	4.3	2670	19
14	s.v.	1.9	0.0	496	11	230	5	0.30	0.05	0.11	0.00	520	12	260.0	2.7	2290	15
15	s.v.	3.5	0.1	325	7	222	5	0.07	0.05	0.13	0.00	290	6	93.0	0.7	1170	8
16	s.v.	4.0	0.4	1040	91	250	28	0.47	0.22	0.02	0.00	1300	130	260.0	5.3	2280	27
17	m.p.	1.1	0.0	739	14	188	4	0.23	0.02	0.27	0.00	730	13	650.0	10.0	3610	26
18	s.v.	3.1	0.0	306	5	440	7	0.23	0.04	0.17	0.00	300	5	100.0	0.7	1240	7
19	matrix	3.6	0.1	395	16	550	22	0.48	0.10	0.05	0.00	480	24	110.0	1.5	1330	13
20	matrix	1.9	0.0	297	2	293	2	0.29	0.01	0.54	0.00	310	2	160.0	1.0	1710	9
21	s.v.	1.9	0.0	946	12	309	6	0.33	0.03	0.19	0.00	1000	13	500.0	2.9	3210	11
22	matrix	2.0	0.0	307	4	337	4	0.27	0.01	0.48	0.01	310	4	150.0	1.0	1670	9
23	matrix	2.2	0.1	301	8	374	10	0.35	0.02	0.15	0.00	330	10	140.0	2.4	1550	19
24	matrix	6.8	0.3	371	17	837	39	0.54	0.03	0.10	0.01	480	29	54.0	0.6	774	7
25	matrix	1.4	0.0	293	4	324	3	0.25	0.00	1.20	0.01	300	4	210.0	2.0	2010	13
26	matrix	1.8	0.1	266	9	357	11	0.29	0.01	0.30	0.01	280	10	150.0	2.4	1620	18
27	matrix	1.8	0.0	383	7	334	18	0.30	0.01	0.59	0.01	400	7	210.0	2.1	2020	14
28	matrix	4.2	0.2	336	20	795	50	0.48	0.03	0.15	0.01	410	29	80.0	1.9	1050	19
29	m.p.	0.7	0.0	448	26	70	4	0.18	0.02	0.17	0.01	430	24	630.0	28.0	3570	69
30	matrix	3.6	0.4	306	39	605	71	0.40	0.06	0.08	0.01	350	49	85.0	4.3	1100	42
31	m.p.	1.3	0.0	362	7	214	4	0.22	0.01	0.67	0.01	360	7	280.0	3.6	2390	18
32	matrix	3.7	0.5	283	40	969	120	0.59	0.08	0.05	0.01	390	70	78.0	5.0	1020	50
32b	matrix	3.6	0.3	268	26	896	76	0.48	0.05	0.09	0.01	330	37	75.0	3.6	1000	37
33	matrix	2.0	0.1	490	21	374	15	0.29	0.02	0.24	0.01	510	22	250.0	4.6	2230	24
34	matrix	3.0	0.2	275	19	428	26	0.33	0.03	0.16	0.01	290	21	92.0	3.0	1160	28
35	m.p.	6.2	1.1	353	67	313	56	0.52	0.10	0.05	0.01	450	110	57.0	3.7	806	43

Extr. No., extraction number; mk, maskelynite; px, pyroxene; fusion, fusion crust; matrix, matrix analyses (maskelynite + pyroxene); m p., melt pocket; s v., shock vein. Amounts of argon are expressed as 10E−12 cc STP. ^{36}Ar concentrations, corrected for cosmogenic ^{36}Ar, yielding negative values are not shown.

Appendix B

Calculation of ^{40}Ar (ppb) and estimation of overpressure in irradiated Martian meteorites

Phase	Extraction No.	^{40}Ar/^{39}Ar corrected	^{40}Ar/K	K$_2$O wt%	K wt%	^{40}Ar (cc STP/g)	^{40}Ar ppb (ppb)	P (bars)
LA001, J = 0.01175 ± 0.0006								
Maskelynite	10	20.7	1.67E−07	0.3	0.2	2.33E−07	0.4	58
	11	15.1	1.22E−07	0.3	0.2	1.70E−07	0.3	43
	12	29.8	2.40E−07	0.3	0.2	3.35E−07	0.6	84
	13	48.2	3.89E−07	0.3	0.2	5.42E−07	1.0	136
	14	149.3	1.20E−06	0.3	0.2	1.68E−06	3.0	420
Melt pocket	6	42.8	3.46E−07	1.0	0.8	1.61E−06	2.9	402
	14b	118.5	9.57E−07	1.0	0.8	4.45E−06	7.9	1112
	16	91.6	7.39E−07	1.0	0.8	3.44E−06	6.1	859
	17	61.1	4.93E−07	1.0	0.8	2.29E−06	4.1	573
	18	107.0	8.64E−07	1.0	0.8	4.02E−06	7.2	1004
	19	131.2	1.06E−06	1.0	0.8	4.92E−06	8.8	1231
	22	96.0	7.74E−07	1.0	0.8	3.60E−06	6.4	900
	24	175.5	1.42E−06	1.0	0.8	6.59E−06	11.8	1647
	25	135.9	1.09E−06	1.0	0.8	5.10E−06	9.1	1275
Zagami, J = 0.00986 ± 0.00005								
Maskelynite	1	39.4	3.18E−07	0.4	0.3	5.92E−07	1.1	148
	2	79.0	6.37E−07	0.4	0.3	1.19E−06	2.1	296
	3	32.6	2.63E−07	0.4	0.3	4.89E−07	0.9	122
	6	34.0	2.75E−07	0.4	0.3	5.11E−07	0.9	128
	8	42.6	3.43E−07	0.4	0.3	6.39E−07	1.1	160
	9	62.9	5.07E−07	0.4	0.3	9.44E−07	1.7	236
	10	128.1	1.03E−06	0.4	0.3	1.92E−06	3.4	481
	12	39.6	3.20E−07	0.4	0.3	5.95E−07	1.1	149
	13	42.2	3.41E−07	0.4	0.3	6.34E−07	1.1	158
	23	40.2	3.24E−07	0.4	0.3	6.03E−07	1.1	151
	24	28.3	2.28E−07	0.4	0.3	4.24E−07	0.8	106
	25	45.8	3.70E−07	0.4	0.3	6.88E−07	1.2	172
	27	54.1	4.36E−07	0.4	0.3	8.12E−07	1.4	203
	28	37.9	3.05E−07	0.4	0.3	5.68E−07	1.0	142
	29	67.8	5.47E−07	0.4	0.3	1.02E−06	1.8	254
Shock vein	15	48.6	3.92E−07	0.2	0.2	3.65E−07	0.7	91
	17	40.7	3.28E−07	0.2	0.2	3.06E−07	0.5	76
	18	51.3	4.14E−07	0.2	0.2	3.85E−07	0.7	96
	19	66.0	5.33E−07	0.2	0.2	4.95E−07	0.9	124
	20	41.2	3.33E−07	0.2	0.2	3.10E−07	0.6	77
	21	33.5	2.71E−07	0.2	0.2	2.56E−07	0.4	63
Melt pocket	22	1157.7	9.34E−06	0.3	0.2	1.30E−05	23.3	3259
	26	806.9	6.51E−06	0.3	0.2	9.08E−06	16.2	2271
NWA 1068, J = 0.00985 ± 0.000								
Matrix	2	34.1	2.75E−07	0.3	0.2	3.83E−07	0.7	96
	3	107.9	8.70E−07	0.3	0.2	1.21E−06	2.2	304
	6	18.4	1.49E−07	0.3	0.2	2.08E−07	0.4	52
	7	14.6	1.18E−07	0.3	0.2	1.64E−07	0.3	41
	8	40.6	3.28E−07	0.3	0.2	4.57E−07	0.8	114

(*continued on next page*)

Appendix B (*continued*)

Phase	Extraction No.	^{40}Ar/^{39}Ar corrected	^{40}Ar/K	K_2O wt%	K wt%	^{40}Ar (cc STP/g)	^{40}Ar ppb (ppb)	P (bars)
	9	17.8	1.44E−07	0.3	0.2	2.00E−07	0.4	50
	10	69.8	5.63E−07	0.3	0.2	7.86E−07	1.4	196
	11	73.4	5.92E−07	0.3	0.2	8.27E−07	1.5	207
	12	13.4	1.08E−07	0.3	0.2	1.51E−07	0.3	38
	13	18.4	1.48E−07	0.3	0.2	2.07E−07	0.4	52
	14	19.2	1.55E−07	0.3	0.2	2.16E−07	0.4	54
	29	23.1	1.86E−07	0.3	0.2	2.60E−07	0.5	65
	30	27.8	2.24E−07	0.3	0.2	3.12E−07	0.6	78
	34	23.4	1.89E−07	0.3	0.2	2.63E−07	0.5	66
Shock vein	15	136.9	1.14E−06	0.2	0.2	1.03E−06	1.8	257
	16	83.3	6.72E−07	0.2	0.2	6.25E−07	1.1	156
	17	92.8	7.49E−07	0.2	0.2	6.97E−07	1.2	174
	18	71.6	5.78E−07	0.2	0.2	5.37E−07	1.0	134
	19	48.9	3.94E−07	0.2	0.2	3.67E−07	0.7	92
	24	111.2	8.97E−07	0.2	0.2	8.35E−07	1.5	209
	25	79.0	6.38E−07	0.2	0.2	5.93E−07	1.1	148
	31	178.2	1.44E−06	0.2	0.2	1.34E−06	2.4	334
Melt pocket	5	263.3	2.12E−06	0.2	0.2	1.98E−06	3.5	494
	20	797.1	6.43E−06	0.2	0.2	5.98E−06	10.7	1496
	21	568.2	4.59E−06	0.2	0.2	4.26E−06	7.6	1066
	22	1087.3	8.77E−06	0.2	0.2	8.16E−06	14.6	2040
	23	612.0	4.94E−06	0.2	0.2	4.59E−06	8.2	1148
	26	611.0	4.93E−06	0.2	0.2	4.59E−06	8.2	1146
	27	382.2	3.08E−06	0.2	0.2	2.87E−06	5.1	717
	32	902.3	7.28E−06	0.2	0.2	6.77E−06	12.1	1693
	33	533.0	4.30E−06	0.2	0.2	4.00E−06	7.1	1000
DaG 476, J = 0.00984 ± 0.00005								
Matrix	1	280.3	2.26E−06	0.1	0.1	1.05E−06	1.9	263
	2	107.6	8.68E−07	0.1	0.1	4.04E−07	0.7	101
	3	71.4	5.77E−07	0.1	0.1	2.68E−07	0.5	67
	4	237.1	1.91E−06	0.1	0.1	8.90E−07	1.6	222
	5	89.3	7.20E−07	0.1	0.1	3.35E−07	0.6	84
	6	79.6	6.43E−07	0.1	0.1	2.99E−07	0.5	75
	8	168.7	1.36E−06	0.1	0.1	6.33E−07	1.1	158
	9	66.7	5.38E−07	0.1	0.1	2.50E−07	0.4	63
	10	139.8	1.13E−06	0.1	0.1	5.25E−07	0.9	131
	19	110.5	8.92E−07	0.1	0.1	4.15E−07	0.7	104
	20	160.2	1.29E−06	0.1	0.1	6.01E−07	1.1	150
	22	154.6	1.24E−06	0.1	0.1	5.80E−07	1.0	145
	23	138.7	1.12E−06	0.1	0.1	5.21E−07	0.9	130
	24	54.5	4.40E−07	0.1	0.1	2.04E−07	0.4	51
	25	207.3	1.67E−06	0.1	0.1	7.78E−07	1.4	194
	26	147.7	1.19E−06	0.1	0.1	5.54E−07	1.0	139
	27	209.7	1.69E−06	0.1	0.1	7.87E−07	1.4	197
	28	80.3	6.48E−07	0.1	0.1	3.01E−07	0.5	75
	30	85.4	6.89E−07	0.1	0.1	3.20E−07	0.6	80
	32	77.5	6.25E−07	0.1	0.1	2.91E−07	0.5	73
	32b	75.3	6.08E−07	0.1	0.1	2.83E−07	0.5	71

	33	247.8	2.00E−06	0.1	0.1	9.30E−07	1.7	232
	34	91.6	7.39E−07	0.1	0.1	3.44E−07	0.6	86
Shock vein	14	259.6	2.09E−06	0.3	0.2	2.92E−06	5.2	731
	15	93.0	7.51E−07	0.3	0.2	1.05E−06	1.9	262
	16	258.4	2.09E−06	0.3	0.2	2.91E−06	5.2	727
	18	100.1	8.08E−07	0.3	0.2	1.13E−06	2.0	282
	21	500.1	4.04E−06	0.3	0.2	5.63E−06	10.0	1408
Melt pocket	13	345.8	2.79E−06	0.1	0.1	1.30E−06	2.3	324
	17	651.4	5.26E−06	0.1	0.1	2.44E−06	4.4	611
	29	632.9	5.11E−06	0.1	0.1	2.38E−06	4.2	594
	31	280.8	2.27E−06	0.1	0.1	1.05E−06	1.9	263

^{40}Ar concentration (cc STP/g) and atmospheric overpressure (bars) have been calculated as follows: $^{40}Ar/^{39}Ar$ ratio: measured in this study using an IR laser probe. $^{40}Ar/K = (^{40}Ar/^{39}Ar \text{ ratio} * J * 0.0001167)/142.6$, where 0.0001167 is the proportion of ^{40}K in natural potassium, which is dominated by ^{39}K (0.93) and ^{41}K (0.07), and 142.6 is a conversion factor to go from cc of ^{39}Ar measured, to g of potassium in the sample. K_2O wt% oxide: individual phases where analyzed for K_2O using EDS. The values given represent an average of 10 analyses per phase (melt pocket, shock vein, maskelynite). $K\% = K_2O \text{ wt\% oxide} * 0.83$. $^{40}Ar \text{ cc STP/g} = (22414 * {}^{40}Ar/K * K\%/100)/40$, where 22414 is the number of cc in a mole of gas and one mole of ^{40}Ar weighs 40 g. $^{40}Ar \text{ ppb} = (^{40}Ar/K * K\%/100) * 1000000000$. Ar overP bars = (^{40}Ar cc STP/g)/(Ar pressure at the Martian surface) * (Ar solubility in basalt), where the atmospheric pressure of Ar at the Martian surface = 1.0^{-4} bars. Ar solubility in basalt = 4.0×10^{-5} cc STP/g per bar.

References

Barrat, J.A., Jambon, A., Bohn, M., Gillet, PH., Sautter, V., Gopel, C., Lesourd, M., Keller, F., 2002. Petrology and chemistry of the Picritic Shergottite North West Africa 1068 (NWA 1068). *Geochim. Cosmochim. Acta* **66**, 3505–3518.

Beck, P., Gillet, P., Gautron, L., Daniel, I., El Goresy, A., 2004. A new natural high pressure (Na, Ca)-hexaluminosilicate $[(Ca_xNa_{1-x})Al_{3+x}Si_{3-x}O_{11}]$ in shocked Martian meteorites. *Earth Planet. Sci. Lett.* **219**, 1–12.

Becker, R.H., Pepin, R.O., 1986. The case for a Martian origin of the shergottites: nitrogen and noble gases in EETA 79001. *Earth Planet. Sci. Lett.* **69**, 225–242.

Bogard, D.D., 1997. A reappraisal of the Martian $^{36}Ar/^{38}Ar$ ratio. *J. Geophys. Res.* **102**, 1653–1661.

Bogard, D.D., Johnson, P., 1983. Martian gases in an Antarctic meteorite? *Science* **221**, 651–654.

Bogard, D.D., Garrison, D.H., 1998. Relative abundances of argon, krypton, and xenon in the Martian atmosphere as measured in Martian meteorites. *Geochim. Cosmochim. Acta* **62**, 1829–1835.

Bogard, D.D., Garrison, D.H., 1999. Argon-39-argon-40 "ages" and trapped argon in Martian shergottites, Chassigny and Allan Hills 84001. *Meteor. Planet. Sci.* **34**, 451–473.

Bogard, D.D., Hörz, F., Johnson, P.H., 1986. Shock-implanted noble gases: an experimental study with implications for the origin of Martian gases in shergottite meteorites. *J. Geophys. Res.* **91** (B13), E99–E114.

Bogard, D.D., Hörz, F., Johnson, P., 1989. Shock-implanted noble gases II: additional experimental studies and recognition in naturally shocked terrestrial materials. *Meteoritics* **24**, 113–123.

Brearly, A.J., 1991. Subsolidus microstructures and cooling history of pyroxenes in the Zagami shergottite. *Lunar Planet. Sci. XXII, Lunar Planet. Inst. Houston*, 135–136 (abstr.).

Carroll, D.S., Draper, R.A., Brooker, R.A., Kelley, S.P., 1994. Noble gas solubilities in melts and crystals. In: Matsuda, J. (Ed.), *Noble Gas Geochemistry and Cosmochemistry*, pp. 325–341.

Catling, D.C., 2006. Atmospheric evolution of Mars. In: Gornitz, V. (Ed.), *Encyclopedia of Paleoclimatology and Ancient Environments*. Kluwer Academic. pp. 1–16.

Crawford, D.A., Barnouin-Jha, O.S., 2003. Mesoscale computational investigation of shocked heterogeneous materials: strength of rocks under impact loading. *Meteor. Planet. Sci.* **39**, A26 (abstr.).

Eugster, O., Busemann, H., Lorenzetti, S., Terribilini, D., 2002. Ejection ages from ^{81}Kr–^{83}Kr dating and pre-atmospheric sizes of Martian meteorites. *Meteor. Planet. Sci.* **37**, 1345–1360.

Fritz, J., Artemieva, N., Greshake, A., 2005. Ejection of Martian meteorites. *Meteor. Planet. Sci.* **40**, 1393–1411.

Garrison, D.H., Bogard, D.D., 2001. Argon-39-argon-40 "ages" and trapped argon for three Martian shergottites. *Meteor. Planet. Sci.* **36**, 62–63 (abstr.).

Haines, P.W., Jenkins, R.J.F., Kelley, S.P., 2001. Pleistocene glass in the Australian desert: the case for an impact origin. *Geology* **29**, 899–902.

Herrmann, W., Berry, R.F., 2002. MINSQ—a least squares spreadsheet method for calculating mineral proportions from whole rock major element analyses. *Geochem. Exp. Environ. Anal.* **2**, 361–368.

Heymann, D., Mazor, E., Anders, E., 1968. Ages of Ca-rich achondrites—I. *Eucrites. Geochim. Cosmochim. Acta* **32**, 1241–1268.

Hohenberg, C.M., Marti, K., Podosek, F.A., Reedy, R.C., Shirck, J.R., 1978. Comparisons between observed and predicted cosmogenic noble gases in lunar samples. *Proc. Lunar Planet. Sci. Conf.* **9**, 2311–2344.

Kenkmann, T., Stöffler, D., Hornemann, U., 2000. Formation of shock-induced pseudotachylites along lithological interfaces. *Meteor. Planet. Sci.* **35**, 1275–1290.

Kieffer, H.H., Jakosky, B.M., Snyder, C.W., 1992. The planet Mars: from antiquity to present. In: Kieffer, H.H., Jakosky, B.M., Snyder, C.W., Mathews, M.S. (Eds.), *Mars*. The University of Arizona Press, Tucson, pp. 1–33.

Jakosky, B.M., Pepin, R.O., Johnson, R.E., Fox, J.L., 1994. Mars atmospheric fractionation by solar-wind-induced sputtering and photochemical escape. *Icarus* **111**, 271–288.

Langenhorst, F., Poirier, J.-P., 2000. Anatomy of black veins in Zagami: clues to the formation of high-pressure phases. *Earth Planet. Sci. Lett.* **184**, 37–55.

Langenhorst, F., Poirier, J.-P., Deutsch, A., Hornemann, U., 2002. Experimental approach to generate shock veins in single crystal olivine by shear melting. *Meteor. Planet. Sci.* **37**, 1541–1553.

Lentz, R.C., McSween Jr., H.Y., 2000. Crystallization of the basaltic shergottites: insights from crystal size distribution (CSD) analysis of pyroxenes. *Meteor. Planet. Sci.* **35**, 919–927.

Lentz, R.C., McSween, H.Y., Jr., 2003. Crystal size distribution analysis of new Nakhlites and Los Angeles: how do they compare with SNC of old? *Lunar Planet. Sci. XXXIV. Lunar Planet. Inst., Houston.* #1914 (abstr.).

Leya, I., Graf, T.H., Nishiizumi, K., Wieler, R., 2001. Cosmic-ray production rates of helium, neon and argon isotopes in H chrondrites based on chlorine-36/argon-36 ages. *Meteor. Planet. Sci.* **36**, 963–973.

Marti, K., Kim, J.S., Thakur, A.N., McCoy, T.J., Keil, K., 1995. Signatures of the Martian atmosphere in glass of the Zagami meteorite. *Science* **267**, 1981–1984.

Mathew, K.J., Marty, B., Marti, K., Zimmerman, L., 2003. Volatiles (nitrogen, noble gases) in recently discovered SNC meteorites, extinct radioactivities and evolution. *Earth Planet. Sci. Lett.* **214**, 27–42.

McCoy, T.J., Lofgren, G.E., 1996. Crystallization of the Zagami shergottite: an experimental study. *Earth Planet. Sci. Lett.* **173**, 397–411.

McCoy, T.J., Taylor, G.J., Keil, K., 1992. Zagami: product of a two-stage magmatic history. *Geochim. Cosmochim. Acta* **56**, 3571–3582.

McCoy, T.J., Wadhwa, M., Keil, K., 1999. New lithologies in the Zagami meteorite: evidence for fractional crystallization of a single magma unit on Mars. *Geochim. Cosmochim. Acta* **63**, 1249–1262.

McDougall, I., Harrison, T.M., 1999. *Geochronology and thermochronology by the* ^{40}*Ar–*^{39}*Ar method*. Oxford University Press.

McSween Jr., H.Y., Jarosewich, E., 1983. Petrogenesis of the Elephant Moraine 79001 meteorite: multiple magma pulses on the shergottite parent body. *Geochim. Cosmochim. Acta* **47**, 1501–1513.

Melosh, H.J., Vickery, A.M., 1989. Impact erosion of the primordial atmosphere of Mars. *Nature* **338**, 487–489.

Meyer, C., 2006. Mars meteorite compendium. http://curator.jsc.nasa.gov/antmet/mmc/index.cfm.

Nier, A.O., 1950. A redetermination of the relative abundances of the isotopes of carbon, nitrogen, oxygen, argon and potassium. *Phys. Rev.* **77**, 789–793.

Nyquist, L.E., Bogard, D.D., Shih, C.-Y., Greshake, A., Stöffler, D., Eugster, O., 2001. Ages and geologic histories of Martian meteorites. *Space Sci. Rev.* **96**, 105–164.

Ostertag, R., Omthauer, G., Rager, H., McSween Jr., H.Y., 1984. Fe^{3+} in shocked olivine crystals of the ALH 77005 meteorite. *Earth Planet. Sci. Lett.* **67**, 162–166.

Ott, U., 2002. Noble gases in meteorites—trapped components. *Rev. Min. Geochem.* **47**, 71–100.

Owen, T., Biemann, K., Rushneck, D.R., Howarth, D.W., Lafleur, A.L., 1977. The composition of the atmosphere at the surface of Mars. *J. Geophys. Res.* **82**, 4635–4639.

Pepin, R.O., Carr, M.H., 1988. Major issues and outstanding questions. In: Kieffer, H.H., Jakosky, B.M., Snyder, C.S., Mathews, M.S. (Eds.), *Mars*. University of Arizona Press, Tucson, pp. 120–143.

Renne, P.R., Swisher, C.C., Deino, A.L., Karner, D.B., Owens, T.L., DePaolo, D.J., 1998. Intercalibration of standards, absolute ages and uncertainties in ^{40}Ar/^{39}Ar dating. *Chem. Geol.* **145**, 117–152.

Rubin, A.E., Warren, P.H., Greenwood, J.P., Verish, R.S., Leshin, L.A., Hervig, R.L., Clayton, R.N., Mayeda, T.K., 2000. Los Angeles: the most differentiated basaltic Martian meteorite. *Geology* **28**, 1011–1014.

Shih, C.-Y., Nyquist, L.E., Wiesmann, H., Barrat, J.A., 2003. Age and petrogenesis of picritic shergottite NWA 1068: Sm–Nd and Rb–Sr isotopic studies. *Lunar Planet. Sci. XXXIV, Lunar Planet. Inst., Houston.* #1439 (abstr.).

Spray, J.G., 1995. Pseudotachylyte controversy: fact or friction? *Geology* **23**, 1119–1122.

Spray, J.G., 1999. Shocking rocks by cavitation and bubble implosion. *Geology* **27**, 695–698.

Stolper, E., McSween Jr., H.Y., 1979. Petrology and origin of the shergottite meteorites. *Geochim. Cosmochim. Acta* **43**, 1475–1498.

Stöffler, D., Keil, K., Scott, E.R.D., 1991. Shock metamorphism of ordinary chondrites. *Geochim. Cosmochim. Acta* **55**, 3845–3867.

Swindle, T.D., Caffee, M.W., Hohenberg, C.M., 1986. Xenon and other noble gases in shergottites. *Geochim. Cosmochim. Acta* **50**, 1001–1015.

Swindle, T.D., 2002. Martian noble gases. In: Rosso, J.J., Ribbe, P.H. (Eds.), Noble gases in geochemistry and cosmochemistry, *Rev. Min. Geochem.* 47, pp. 171–190.

Takata, T., Ahrens, T.J., 1995. Atmospheric effects on cratering on Venus. *J. Geophys. Res.* **100** (E11), 23329–23348.

Terribilini, D., Eugster, O., Burger, M., 1998. Noble gases and chemical composition of Shergotty mineral fractions, Chassigny, and Yamato 793605: the trapped argon-40 argon-36 ratio and ejection times of Martian meteorites. *Meteor. Planet. Sci.* **33**, 677–684.

Terribilini, D., Busemann, H., Eugster, O., 2000. ^{81}Kr–Kr cosmic-ray exposure ages of Martian meteorites including the new shergottite Los Angeles. *Meteor. Planet. Sci.* **35**, A155 (abstr.).

Thompson, L.M., Spray, J.G., 1996. Pseudotachylyte petrogenesis: constraints from the Sudbury impact structure. *Contrib. Min. Pet.* **125**, 359–374.

Treiman, A.H., McKay, G.A., Bogard, D.D., Mittlefehldt, D.W., Wang, M.-S., Keller, L., Lipschultz, M.E., Lindstrom, M.M., Garrison, D., 1994. Comparison of LEW88516 and ALH77005 Martian meteorites: similar but distinct. *Meteoritics* **29**, 581–592.

Tuchscherer, M.G., Spray, J.G., 2002. Geology, mineralization, and emplacement of the Foy offset dike, Sudbury impact structure. *Econ. Geol. Bull. Soc.* **97**, 11377–11397.

Turner, G., Knott, S.F., Ash, R.D., Gilmour, J.D., 1997. Ar-Ar chronology of the Martian meteorite ALH84001: evidence for the timing of the early bombardment of Mars. *Geochim. Cosmochim. Acta* **61**, 3835–3850.

van der Bogert, C.H., Schultz, P.H., Spray, J.G., 2003. Impact-induced frictional melting in ordinary chondrites: a mechanism for deformation, darkening and vein formation. *Meteor. Planet. Sci.* **38**, 1521–1532.

Walton, E.L., Herd, C.D.K., 2006. Localized shock melting in Northwest Africa 1950: comparison with ALH 77005. *Meteor. Planet. Sci.* in press.

Walton, E.L., Spray, J.G., 2003a. Localized shock excursions in Martian meteorites: the Los Angeles basaltic shergottite and Northwest Africa 1068 olivine-phyric shergottite. In: Dressler, B. (Ed.), *Third International Conference on Large Meteorite Impacts*, Lunar Planet. Inst., Houston. #4097 (abstr.).

Walton, E.L., Spray, J.G., 2003b. Mineralogy, microtexture, and composition of shock-induced melt pockets in the Los Angeles basaltic shergottite. *Meteor. Planet. Sci.* **38**, 1865–1875.

Walton, E.L., Spray, J.G., Bartoschewitz, R., 2005. A new Martian meteorite from Oman: mineralogy, petrology and shock metamorphism of olivine-phyric basaltic shergottite Sayh al Uhaymir 150. *Meteor. Planet. Sci.* **40**, 1195–1214.

Wieler, R., 2002. Cosmic-ray produced noble gases in meteorites. *Rev. Min. Geochem.* **47**, 125–170.

Wiens, R.C., 1988. On the siting of gases shock-emplaced from internal cavities in basalt. *Geochim. Cosmochim. Acta* **52**, 2775–2783.

Wiens, R.C., Pepin, R.O., 1988. Laboratory shock emplacement of noble gases nitrogen, and carbon dioxide into basalt, and implications for trapped gases in shergottite EETA79001. *Geochim. Cosmochim. Acta* **52**, 295–307.

Wiens, R.C., Becker, R.H., Pepin, R.O., 1986. The case for a Martian origin of the shergottites, II. Trapped and indigenous gas components in EETA 79001 glass. *Earth Planet. Sci. Lett.* **7**, 149–158.

Xirouchakis, D., Draper, D.S., Schwandt, C.S., Lanzirotti, A., 2002. Crystallization conditions of Los Angeles, a basaltic Martian meteorite. *Geochim. Cosmochim. Acta* **66**, 1867–1880.

Zipfel, J., Scherer, P., Spettel, B., Dreibus, G., Schultz, L., 2000. Petrology and chemistry of the new shergottite Dar al Gani 476. *Meteor. Planet. Sci.* **35**, 95–106.